REVIEW

Check for updates

Analytical techniques for studying cell aging in lithium–sulfur batteries

Ritu Malik, Vijay K. Tomer [ID] * and Mohini Sain

Lithium–sulfur batteries (LiSBs) hold promise for future energy storage due to their high theoretical energy density, but practical use faces challenges like capacity loss, short cycle life, and poor rate performance, primarily due to sulfur's complex redox reactions and polysulfide dissolution. Despite these challenges affecting LiSBs' lifespan and durability, post-mortem analysis of aged cells with physico-chemical techniques is increasingly essential for studying batteries, identifying new species, and monitoring electrode health and energy stability. This review explores the literature on analyzing aged LiSBs, encompassing disassembly methodologies and techniques (microscopic, spectroscopic, and electrochemical) to characterize materials retrieved from aged batteries. This discussion explores how these techniques have been crucial in studying structural, morphological, and chemical changes in LiSBs during cycling, highlighting key findings and insights, while also addressing challenges and future directions in post-mortem analysis, emphasizing the need for advanced analytical methods and multi-modal approaches to unravel complex degradation mechanisms, ultimately advancing the LiSBs.

Broader context

Reviewing post-mortem analytical techniques in lithium–sulfur batteries (LiSBs) provides a comprehensive understanding of the complex degradation mechanisms that limit their performance and longevity. By reviewing post-mortem analytical techniques, the most effective methods for studying LiSB degradation can be identified, including changes in structure, morphology, and chemistry. This knowledge can lead to the development of strategies to mitigate degradation, such as optimizing electrode/separator design, electrolyte composition, and cycling conditions. Additionally, the review provides insights into the broader field of battery research, highlighting the basic principles of analytical techniques and key insights in understanding battery degradation. This information can guide future research directions, such as the development of new analytical tools and techniques for studying other types of batteries. Overall, this comprehensive overview of the post-mortem analytical techniques in LiSBs offers valuable insights for researchers working to improve the performance and longevity of these promising energy storage devices with implications for improving the performance, safety, and sustainability of battery systems.

1. Introduction

Batteries, which convert chemical energy into electricity, are crucial for devices like portable electronics, satellites, medical equipment, EVs, and renewable energy systems, and expanding their market requires improving electrochemical performance, lifespan, cost efficiency, and environmental impact.[1–5] Lithium–sulfur batteries (LiSBs) stand out among current chemistries for their high potential in technological applications, offering exceptional specific capacity and cost-effective

Department of Mechanical & Industrial Engineering, University of Toronto, Canada.
E-mail: vj.kumar@utoronto.ca

materials, with theoretical specific energy and volumetric energy densities around 2600 W h kg^{-1} and 2800 W h L^{-1}—2 to 6 times greater than the limits of advanced commercial lithium-ion batteries (LIBs).[6–9] Despite their high energy density, abundant precursors, and cost-effectiveness, LiSBs face commercialization challenges, including sulfur's poor conductivity and discharge species (lithium polysulfides, LiPS) leading to high electrochemical polarization and impedance, with LiPS diffusing into the electrolyte and reacting with the anode (shuttle effect), and sulfur cathode volume changes causing pulverization and detachment from conductive substrates.[10–13] In addition, advancing LiSBs requires enhancing lifespan, fast charging, low-temperature performance, self-recovery, and safety while addressing issues like lithium

plating, cathode pulverization, microstructural loss, and chemical degradation, making a thorough understanding of these mechanisms crucial for optimal design and safe operation.[14,15]

The redox chemistry of LiSBs is more complex than LIBs, involving solid-state S8 and lower-ordered LiPSs (Li_2S_2/Li_2S), while long-chain LiPSs dissolve in the electrolyte, causing the sulfur cathode to transition from solid to liquid and back during cycling, leading to significant challenges.[16–18] Despite significant progress, gaps remain in fully understanding battery degradation, such as side reactions during cycling, aging, and material-level chemical breakdowns, leading to capacity loss and increased resistance, making it essential to grasp these mechanisms to enhance cell lifespan. Electrochemical methods such as cyclic voltammetry, galvanostatic cycling, EIS, and rate capability tests are used to explore reaction mechanisms and evaluate battery performance, linking macroscopic behavior with LiSBs' internal design for optimal composition and structure; however, since these measurements alone can't fully uncover reaction pathways or microscopic electrode changes, turning the battery into a "black box", in situ and operando techniques are employed to study real-time reaction mechanisms and sulfur cathode state changes.[19–27] Compared to the operando methods, the post-mortem analytical techniques offer distinct advantages over the operando methods for analyzing the operation and degradation of LiSBs, particularly after cycling or aging.[28,29] LiSBs involve complex electrochemical processes, including the polysulfide shuttle, sulfur dissolution, and the formation of insulating Li_2S during discharge. These processes contribute to capacity fading and induce structural and chemical transformations that are difficult to capture in real-time.[30] Operando techniques, which provide valuable real-time insights into dynamic processes such as phase transitions, lithium-ion transport, and electrode–electrolyte interactions, often face limitations in spatial and temporal resolution due to the constraints of observing these changes while the battery is actively cycling.[31–33] As a result, long-term degradation phenomena, such as irreversible sulfur species deposition or gradual electrode degradation, may go undetected. In contrast, postmortem analysis enables the detailed disassembly and examination of battery components after operation, providing a comprehensive understanding of cumulative degradation and failure modes. Because the battery is no longer operating, postmortem techniques can dismantle and closely examine battery components without concern for disrupting ongoing processes. Techniques such as scanning electron microscopy (SEM), X-ray photoelectron spectroscopy (XPS), and energy-dispersive X-ray spectroscopy (EDX) allow for the thorough investigation of electrode surfaces, residual sulfur species, and degradation products like LiPSs.[34–38] Postmortem methods are highly effective at uncovering long-term degradation in lithium–sulfur batteries, revealing microstructural changes, electrolyte decomposition, and passivation layers that are not easily detected during operation. Postmortem analysis excels at identifying slower degradation processes like dendrite

growth, particle cracking, and SEI evolution.[28] By allowing battery disassembly, it provides a clearer understanding of failure modes such as material dissolution, lithium plating, inactive phase accumulation, and structural damage, making it more suitable for diagnosing root causes of failure after extended cycling.[39,40] The increasing interest in examining aged LiSBs (Scheme 1) with various tools highlights the need for standardized procedures in cell opening, components (electrodes and separators, etc.) recovery, sample processing, and analysis to ensure accurate and reliable data while minimizing damage and contamination.

In this review, we cover advanced physicochemical methods for analyzing various components of aged LiSBs, addressing a gap in the literature where existing reviews on in situ and operando techniques for LiSBs have not concentrated on post-mortem analysis.[41–43] As the first review in this direction, we outline the underlying principle for electrochemical approaches, microscopic, X-ray-based spectroscopic, and optical spectroscopic techniques (Scheme 2). These methods help understand degradation mechanisms in LiSBs and provide successful examples demonstrating the information derived from these techniques and their applications in the battery field (Table 1). We also discuss the latest methods which have been explored to analyze LIBs but not for LiSBs, highlighting the crucial gap in current post-mortem approach and suggesting future directions to enhance understanding of LiSBs.

2. Standard procedure for cell opening

Scheme 3 outlines the steps in post-use cell analysis, where non-destructive methods like CV and EIS provide initial
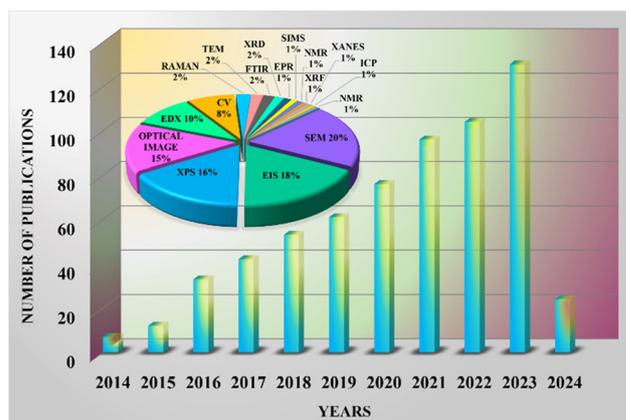
Scheme 1 Number of research publications involving post-mortem analysis in LiSBs (search term: "lithium−sulfur batteries + post-mortem analysis + cycled cell") in last 10 years. Data was obtained from the Web of Science on February 25, 2024. The inset pie chart indicates the tentative %share of each analytical technique in a total number of publications.
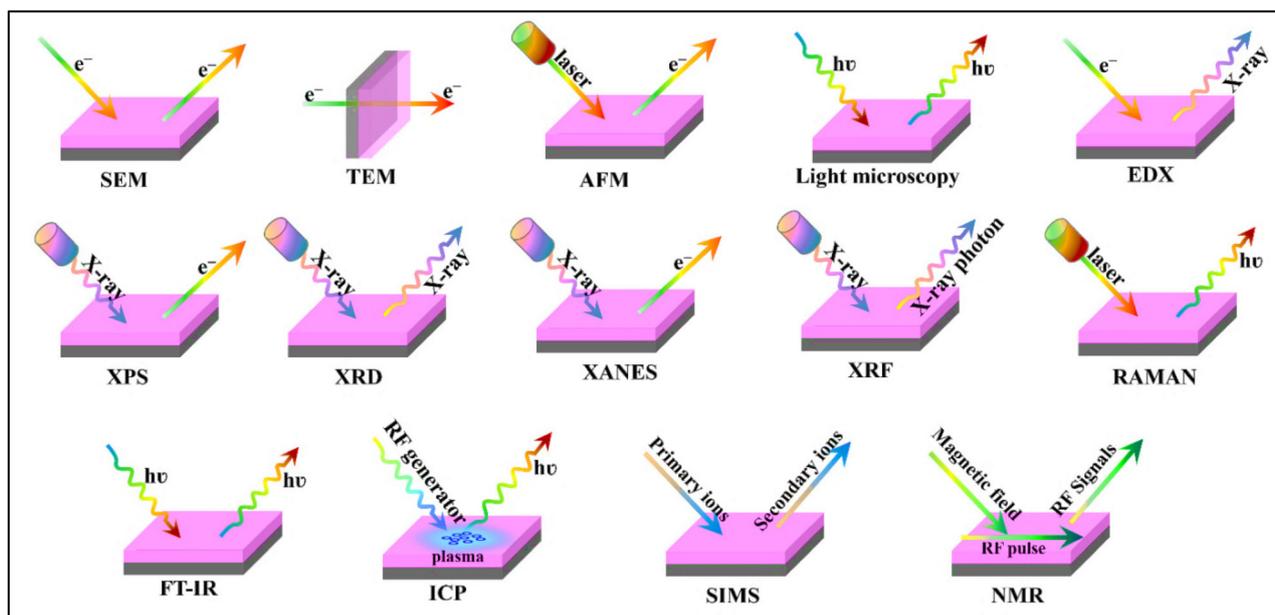
Scheme 2 Simplified diagrams of detected particles using various analysis methods.

insights into aging mechanisms before disassembly, but direct observation of chemical changes requires opening the cell (Scheme 4).[19,44] Localized aging phenomena, often missed in averaged electrochemical measurements, necessitate crucial steps before cell opening, like charging or discharging to a specific state of charge (SOC).[45–47] To ensure safety, deep discharge to 0 V is recommended, as it lowers energy content and minimizes the risk of thermal runaway in the event of a short circuit.[48] Since some LiSB components react with O_2 and H_2O, a glove box with a high-purity Ar atmosphere (<0.1 ppm H_2O and O_2) is essential, and precautions must be taken during cell opening to prevent internal short circuits, which are most likely when cutting the cell housing or applying mechanical pressure to the electrode stack or jelly roll.[49] After separating the cell components, electrolyte solvents like DME or DOL are used to clean to eliminate residual crystallized LiPSs or non-volatile solvents that could be confused with SEI elements or intercalated Li.[49]

3. Post-mortem characterization techniques

3.1. Electrochemical methods

Post-mortem characterization of LiSBs using electrochemical methods involves analyzing the electrochemical behavior of the cell components after cycling (before cell disintegration) to understand the behavioral changes and deviation from the fresh cells.[20,22] Some key electrochemical methods for post-mortem characterization of LiSBs include:

3.1.1 Electrochemical impedance spectroscopy (EIS). EIS examines battery electrical properties by applying a small sinu-

soidal current or voltage across different frequencies, measuring the output's amplitude and phase shift to create an impedance spectrum.[53–55] In LiSBs, EIS evaluates impedance at different frequencies to reveal sulfur redox kinetics, charge transfer, and polysulfide dynamics, with impedance shifts during cycling indicating degradation such as insulating layer formation or active material loss.[19,56] Nyquist plots, which graphically depict EIS data, usually show a semicircle for charge transfer resistance at the interface (electrode/electrolyte) and a linear region for Li⁺ diffusion, revealing insights into charge transfer, diffusion, and other electrochemical phenomena in the battery.[53] Wu *et al.* used EIS to examine the impact of electrolyte dilution on LiSB performance, finding that a 0.1 mol L⁻¹ LiTFSI in DME/DOL with 1 wt% $LiNO_3$ significantly improved electrode wetting and boosted the electrochemical performance of high sulfur-loading cathodes while being more cost-effective, lighter, and less viscous compared to commonly used 1 M electrolyte.[50] EIS results (Fig. 1a and b) demonstrated that the 0.1 M electrolyte significantly reduced long-chain polysulfide shuttle by causing Li⁺ cations to form large phase-separated Li_2S_2 domains and preventing the dissolution of short-chain polysulfides, with Li_2S_4 aggregations also slowing the diffusion of both Li_2S_2 and Li_2S_4, suggesting that dilute electrolytes could be more effective for optimizing LiSB performance.

Similarly, Wang *et al.* utilized electrospinning and base-coating to create a flexible fibrous membrane that combines the cathode, interlayer, and separator into a single composite, improving polysulfide confinement, electron transfer, and Li⁺ diffusion while resolving interface issues.[51] This LiSB starts with a capacity of 1501 mA h g⁻¹ and retains 933 mA h g⁻¹ after 400 cycles with minimal loss (0.069% per cycle), and

Table 1 Summary of techniques reported in this review for the analysis of aging LiSBs. A single star (*) represents an estimated amount of 25k CA$

Method	Applications and benefits	Drawbacks	Equipment cost	Time consumed
Electrochemical impedance spectroscopy (EIS)	• EIS accurately assesses battery health through internal resistance measurements. • It provides real-time monitoring of the state of charge and health. • EIS identifies specific degradation mechanisms affecting battery performance. • It optimizes battery design by analyzing impedance contributions from components. • EIS evaluates thermal stability, enhancing safety and preventing thermal runaway.	• Struggles to distinguish between overlapping processes like SEI formation and LIPSs migration. • Limited frequency range reduces accuracy in detecting early dendrite growth. • May not fully capture rapid electrode degradation or transient phenomena. • Electrode polarization effects can obscure subtle impedance changes during cycling. • Complex interpretation of overlapping signals from polysulfides and SEI layer. • Less sensitive to detecting minor structural changes or local electrode defects.	*	~1 h
Cyclic voltammetry (CV)	• CV evaluates lithium intercalation and deintercalation reversibility in batteries. • Measures peak currents and potentials to analyse electrochemical processes. • Provides insights into the stability of electrode materials during cycling. • It assesses capacity retention and efficiency in fresh and cycled batteries. • Aids in optimizing electrolyte formulations for enhanced performance.	• Lacks detailed insights into solid-state processes within the electrode bulk. • Ineffective in detecting dendrite formation or early-stage lithium-metal deposition. • Insufficient for tracking high-rate or variable current behaviors during cycling. • Limited sensitivity to SEI layer evolution, especially under dynamic cycling conditions. • Poor resolution for distinguishing between polysulfide formation and side reactions. • Does not provide comprehensive information on electrode degradation or microstructural defects.	*	1–2 h for a fast scan 2–3 days for a slow scan rate
Scanning electron microscopy (SEM)	• Visualizes multi-dimensional structures in lithium-ion and lithium–sulfur batteries. • Reveals details of crack formation in electrode materials during cycling. • Provides insights into morphological changes affecting battery performance over time. • Enables assessment of surface features and porosity in electrode materials. • Helps evaluating the electrolyte interactions with electrodes under different conditions. • Assists in understanding degradation mechanisms in fresh and cycled batteries	• Can damage e-beam-sensitive materials, such as the SEI layer. • Limited in providing chemical composition details, crucial for analyzing polysulfide formation. • Inability to directly detect lithium ions or track dendrite growth beneath the surface. • Poor resolution for capturing dynamic electrode changes during cycling or side reactions. • Ineffective in visualizing early-stage electrode degradation or microstructural defects. • Requires sample preparation that may alter the native morphology of sensitive materials	*****	1–2 h for sample preparation and analysis
Transmission electron microscopy (TEM)	• Provides detailed insights into particle morphology in batteries. • Analyzes crystallinity to assess material quality and stability. • Reveals stress distributions within electrode materials during battery operation. • Identifies magnetic domains, enhancing understanding of material properties. • Helps investigate phase changes in fresh and cycled batteries. • Facilitates the study of nanoscale structural changes impacting battery performance	• Only scans small sample areas, limiting analysis of larger electrode structures. • Sample preparation can alter the SEI layer and disrupt lithium-ion or polysulfide dynamics. • Less effective for detecting bulk dendrite formation or large-scale electrode degradation. • Difficult to capture real-time structural changes during cycling, especially for side reactions. • High-vacuum conditions can induce material modifications, especially in sensitive sulfur or lithium components. • Limited ability to provide chemical state information crucial for understanding electrode–electrolyte interactions.	*******	1–2 h for sample preparation and analysis

Table 1 (Contd.)

Method	Applications and benefits	Drawbacks	Equipment cost	Time consumed
Atomic force microscopy (AFM)	• Assesses surface roughness of active materials in batteries. • Provides particle size distribution for improved material characterization. • Reveals morphology changes of electrode materials during cycling processes. • Analyzes solid electrolyte interphase (SEI) deposition on lithium anodes. • Aids in understanding the relationship between structure and performance. • Enhances insights into nanoscale features affecting battery efficiency and stability	• Lacks real-time data on lithium-ion dynamics and electrolyte interactions during cycling. • Time-consuming process with limited ability to capture rapid electrode degradation or polysulfide formation. • Inefficient for analyzing bulk properties like dendrite growth or large-scale electrode defects. • Provides no chemical composition information on SEI layer, polysulfides, or side reactions. • Limited resolution for detecting nanoscale features such as lithium-ion transport pathways. • Cannot effectively measure internal structural changes or interactions within the battery electrodes.	****	~1–2 h
Optical imaging	• Provides visual analysis of electrode degradation in batteries. • Captures color changes indicating chemical reactions during cycling. • Allows for the examination of macroscopic defects in active materials. • Optical images help assess the uniformity of electrode coatings. • Facilitates monitoring of interface interactions between electrodes and electrolytes. • Aids in evaluating overall battery performance and stability over time.	• Limited resolution prevents detailed visualization of SEI layer formation and degradation. • Cannot detect nanoscale defects like dendrite growth or subtle electrode surface changes. • Inadequate for observing molecular-level interactions or side reactions, such as polysulfide shuttling. • Unable to capture small cracks or morphological changes during lithium-ion cycling. • Lacks chemical information on lithium-ion migration or electrode composition. • Ineffective for real-time analysis of rapid degradation processes in lithium–sulfur batteries.	*	~0.5 h
X-ray photoelectron spectroscopy (XPS)	• Identifies surface compositions of electrode materials in batteries. • Determines oxidation states to reveal chemical changes during cycling. • Analyzes electronic structures at the electrode/electrolyte interface for performance insights. • Characterizes SEI formation and its impact on cycling. • Detects impurities that may adversely affect battery efficiency. • Provides information on surface functional groups influencing electrode behavior. • It helps monitor degradation processes in fresh and cycled batteries.	• Limited to surface analysis, providing no depth-resolved information on SEI or dendrites. • Cannot detect lithium-ion migration or polysulfide formation occurring beneath the surface. • Costly instrumentation and high-vacuum requirements complicate *in situ* or *operando* analysis. • Sensitivity to surface contamination may skew results in cycled lithium–sulfur batteries. • Ineffective in capturing fast, dynamic changes like electrolyte degradation or side reactions. • Difficult to analyze materials with complex or mixed oxidation states due to overlapping signals.	*******	~3–4 h
X-ray diffraction (XRD)	• Tracks crystal changes in sulfur during battery cycling. • Identifies phase transitions in lithium polysulfides (LiPS) over time. • Analyzes the structural stability of electrode materials throughout cycling. • Provides insights into crystallinity changes affecting battery performance. • Helps determine the optimal composition of electrode materials. • Aids in understanding the effects of cycling on material properties.	• Unable to detect soluble LiPSs during battery cycling or degradation. • Lacks sensitivity to amorphous SEI layer formation and dendrite initiation on the lithium anode. • Provides insufficient information on early-stage electrochemical changes in sulfur cathode. • Ineffective in analyzing side reactions or subtle structural defects in cycled electrodes. • Limited to crystalline phases, missing vital information on electrolyte breakdown or degradation. • Fails to capture dynamic real-time changes during charge–discharge cycles in LiSBs.	****	~1–2 h (slow scan)

Table 1 (Contd.)

| Method	Applications and benefits	Drawbacks	Equipment cost	Time consumed
X-ray absorption near edge spectroscopy (XANES)	• Reveals electronic structures of metallic ions. • Analyzes the chemical states of metals in battery electrodes. • Provides insights into lithium coordination environments and bonding characteristics. • Helps identify redox reactions occurring in electrodes during cycling. • Aids in understanding degradation mechanisms affecting battery performance over time.	• Limited spatial resolution hinders detailed analysis of local chemical environments in electrodes. • Insufficient sensitivity to detect low-concentration species like polysulfides or lithium dendrites. • Unable to provide comprehensive insights into SEI layer characteristics and formation dynamics. • Challenges in differentiating between closely related oxidation states during electrode degradation. • Requires extensive sample preparation, potentially altering the native state of materials. • Does not capture transient or dynamic processes during charge–discharge cycles effectively.	*******	~2–3 h
X-ray fluorescence spectroscopy (XRF)	• Provides quantitative elemental analysis of battery materials. • Analyses the distribution of elements within battery components. • Helps identify impurities that may impact battery performance. • Evaluates the composition of electrode materials in fresh and cycled batteries. • Assists in monitoring changes in elemental concentrations during cycling. • Supports the development of advanced materials by analyzing elemental ratios.	• Limited sensitivity to low atomic number elements like 'lithium' hinders analysis. • Complex sample preparation may alter material properties before analysis occurs. • Inability to provide detailed information on local chemical environments in electrodes. • Does not detect soluble polysulfides or transient species during electrochemical processes. • May struggle to differentiate between overlapping spectral lines in complex mixtures. • Surface analysis only, potentially missing important information from the bulk material.	***	~1–1.5 h
Raman spectroscopy	• Detects molecular vibrations of sulfur and polysulfides in batteries. • Provides insights into the chemical bonding and structure changes. • Helps monitor the formation and dissolution of polysulfides. • Identifies phase transitions in sulfur during cycling processes. • Enables real-time monitoring of electrochemical reactions in batteries. • Assists in evaluating the stability of electrode materials.	• Weak scattering signals from soluble polysulfides limit detection sensitivity and accuracy. • Cannot effectively identify structural changes occurring within the SEI layer. • May struggle to resolve overlapping peaks in complex material spectra. • High laser intensity can cause thermal degradation of sensitive battery materials. • Limited spatial resolution may miss fine details of electrode degradation. • Inability to analyze bulk properties of materials restricts comprehensive understanding.	**	~0.5 h
Fourier Transformation Infra-red (FTIR) spectroscopy	• Detects surface functional groups in battery materials and electrodes. • Identifies fragmented molecules resulting from electrochemical reactions. • Helps monitor changes in the SEI. • Provides insights into electrolyte decomposition and stability during cycling. • Aids in understanding chemical interactions between electrode materials and electrolytes. • Assists in evaluating the effectiveness of additives in improving performance.	• Inability to differentiate among various carbon species complicates analysis. • Limited detection of low-concentration species may overlook critical reactions. • Weak signals from solid-state materials can hinder accurate interpretation. • Cannot provide detailed information on three-dimensional electrode structures. • Requires extensive sample preparation that may alter material properties. • Poor spatial resolution limits the analysis of localized degradation phenomena.	**	~0.5 h

Table 1 *(Contd.)*

Method	Applications and benefits	Drawbacks	Equipment cost	Time consumed
Energy dispersive X-ray spectroscopy (EDX)	• Verifies the elemental composition of active materials in batteries. • Detects additional phases, enhancing understanding of material interactions. • Facilitates spatial mapping of element distributions within electrode structures. • Provides quantitative analysis of elemental ratios critical for performance optimization. • Assists in identifying contaminants that may degrade battery efficiency. • Enables characterization of morphological changes in cycled battery components	• Inability to detect lithium limits comprehensive analysis of battery materials. • Requires complementary techniques like SEM or TEM for effective operation. • Poor sensitivity to light elements complicates understanding of SEI layers. • Limited spatial resolution restricts analysis of microstructural changes in electrodes. • Elemental mapping can be hindered by overlapping X-ray signals. • Surface contamination may significantly affect quantitative compositional analysis accuracy.	***	~1–2 h
Inductive coupled plasma -atomic emission spectroscopy (ICP-AES)	• Detects new materials migrating from the cathode to the anode. • Quantitatively analyzes trace elements in battery components. • Provides insights into contamination sources affecting battery performance. • Characterizes ionic species in electrolytes during charge–discharge cycles. • Enables detailed analysis of elemental leaching processes in batteries. • Assists in evaluating the effectiveness of protective coatings on electrodes	• Limited depth profiling restricts understanding of layer-specific composition changes. • Lack of information on sample morphology complicates analysis of electrode defects. • Inability to detect soluble lithium polysulfides hinders comprehensive battery assessment. • Cannot differentiate between oxidation states of transition metal ions present. • Requires extensive sample preparation, potentially altering the material's characteristics. • Sensitivity to volatile components may lead to inaccuracies in elemental quantification.	*****	~1–1.5 h
Electron paramagnetic resonance (EPR)	• Detects and quantifies paramagnetic species like radicals in battery systems. • Identifies transition metal ions influencing battery degradation mechanisms. • Provides insights into reactive intermediates formed during electrochemical reactions. • Aids in characterizing the impact of impurities on battery performance. • Analyzes spin states that correlate with charge transport processes. • Facilitates understanding of radical formation and stabilization in batteries	• Limited sensitivity to paramagnetic species restricts detection of critical intermediates. • Low operating temperatures fail to simulate actual battery operating conditions. • Inability to quantify species affects understanding of degradation mechanisms. • Difficulty in analyzing complex multi-species systems complicates interpretation of results. • Time-consuming sample preparation may alter the state of the electrodes. • Requires advanced equipment and expertise, increasing operational costs and complexity.	****	~1–1.5 h
Secondary-ion mass spectrometry (SIMS)	• Provides detailed analysis of the SEI layer's elemental composition. • Characterizes molecular species present on battery material surfaces. • Enables depth profiling to study SEI layer development over cycles. • Quantifies lithium distribution within electrodes, revealing interfacial dynamics. • Assists in identifying degradation products influencing battery performance. • Facilitates spatial mapping of elemental compositions across surfaces	• Poor focusing capability leads to reduced spatial resolution in analyses. • Difficult quantification limits accurate determination of elemental concentrations. • Sophisticated electronics increase complexity and maintenance costs of the system. • Sample damage during analysis may alter the state of electrodes. • Limited detection of lighter elements like lithium complicates comprehensive analysis. • Time-intensive sample preparation can hinder rapid assessments of battery performance.	*******	~1–1.5 h

Table 1 *(Contd.)*

| Method	Applications and benefits	Drawbacks	Equipment cost	Time consumed
Nuclear magnetic resonance (NMR) spectroscopy	• Elucidates the dynamics and diffusion properties of lithium ions. • Provides insights into the formation and composition of the SEI. • Characterizes the local environment of lithium in various phases. • Allows for the monitoring of solvent interactions with lithium species. • Enables the analysis of molecular mobility within electrode materials. • Helps identify structural changes during battery cycling processes.	• Expensive experimental setup limits accessibility for routine battery analysis. • Inability to capture dynamic processes during battery operation hinders insights. • Limited sensitivity to sulfur species restricts analysis of key battery components. • Low resolution may miss crucial details in electrode degradation phenomena. • Sample preparation can alter the state of materials, affecting results. • Long acquisition times reduce throughput for analyzing multiple samples efficiently.	********	~1–1.5 h
N_2-sorption isotherms	• Provide quantitative data on the surface area of electrodes. • Measures pore volume, critical for ion transport analysis. • Elucidates the accessibility of electrolytes to electrode materials. • Enables characterization of porosity, influencing overall battery performance. • Assesses structural stability and changes during cycling. • Helps optimize electrode design for enhanced lithium-ion diffusion.	• Lack of electrochemical information limits understanding of ion transport dynamics. • Does not provide insights into the stability of SEI layers formed. • Cannot directly correlate surface area with performance in cycling conditions. • Limited detection of microstructural defects affecting lithium-ion mobility. • Does not account for changes in morphology during battery cycling. • Inability to analyze real-time effects of polysulfides on electrode structure.	**	6–8 h for degassing and 1–2 h for BET analysis
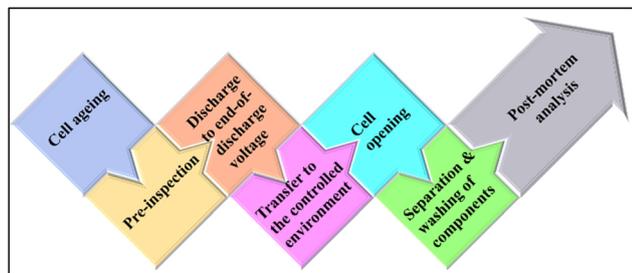
Scheme 3 Flowchart for LiSB disassembly and component analysis.

demonstrates a consistent R_{ct} reduction (Fig. 1c) from 16.86 Ω to 2.30 Ω, reflecting enhanced stability, better efficiency in electron and ion transfer, and improved sulfur redox kinetics. Wei *et al.*[52] reported increased R_{ct} after 100 cycles (Fig. 1d) and better Li$^+$ conductivity using a 3D-printed N-doped Ti$_3$C$_2$ MXene framework (Fig. 1e), which acts as a sulfur host and lithium dendrite blocker. The 3D structure's porosity enhances charge transport and provides ample sulfur redox sites, while the N-pTi$_3$C$_2$T$_x$ layer at the anode supports Li$^+$ deposition, prevents dendrite formation, and ensures consistent Li stripping/ plating due to enhanced lithiophilicity and stable SEI from fluorine groups. The composite cell shows reduced interfacial resistance and improved Li$^+$ conductivity, with decreasing impedance over cycles, indicating better conductivity and SEI stability.

3.1.2 Cyclic voltammetry (CV). CV is an electrochemical technique that examines redox reactions and material properties by applying a voltage to the electrode and measuring

the resulting current, generating a voltammogram through voltage sweeping.[59,60] In LiSBs, this method analyzes sulfur redox processes during charge–discharge cycles, providing insights into reaction kinetics, reversibility, SEI formation, interface stability, and the buildup of insulating products on the electrode.[60,61] By analyzing the CV data, the electrode and electrolyte compositions, cycling conditions, and cell design, the performance and longevity of LiSBs can be optimized, and also understand critical factors that contribute to their degradation over time. The CV data from Huang *et al.*[57] show that using an rGO-coated separator with a cross-linked CMC-CA binder, Toray carbon paper current collector, and reduced graphene oxide (rGO) improves LiSB electrochemical performance by exhibiting higher reduction potentials and lower oxidation potentials (Fig. 2a). Their study also reveals that high sulfur loading leads to increased battery resistance and obstructed ion transport due to insulating sulfur/lithium sulfide deposition, which diminishes sulfur utilization and accelerates capacity decay, while the aggravated shuttle effect and large lithium anode volume changes cause repeated SEI destruction and continuous LiNO$_3$ consumption, resulting in infinite charging issues. Similarly, Huang *et al.*[58] observed that composite cathodes, utilizing a saccharide-based binder system, showed higher cathodic and anodic peak magnitudes (Fig. 2b) after 20 cycles, indicating improved lithiation and delithiation kinetics. This binder system, which controls polysulfides due to its reducing properties and forms a web-like microstructure in the sulfur cathode, achieved 97% sulfur utilization, a lifespan of 1000 cycles, and high-capacity retention (1106 mA h g^{-1} after 500 cycles). Additionally, the reduction peaks for this binder
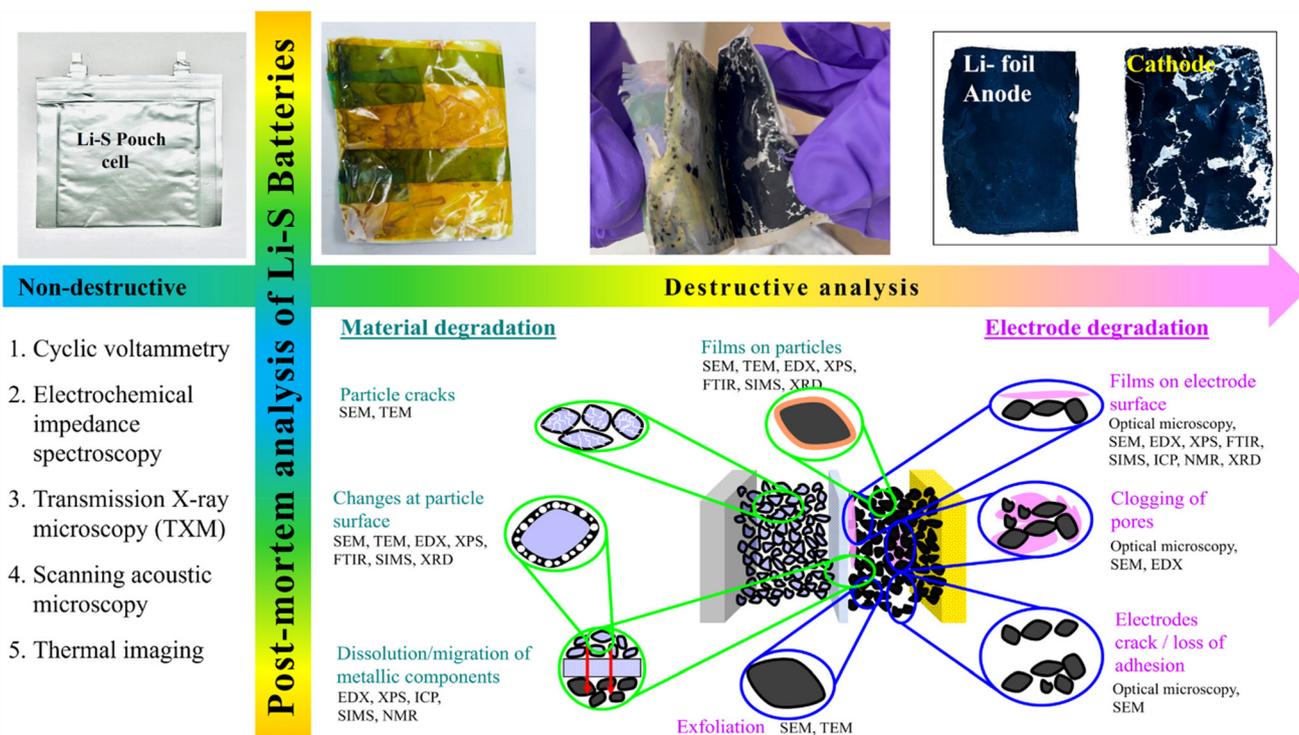
Scheme 4 Illustrative image of a Li–S pouch cell prepared in our lab and its disintegration.
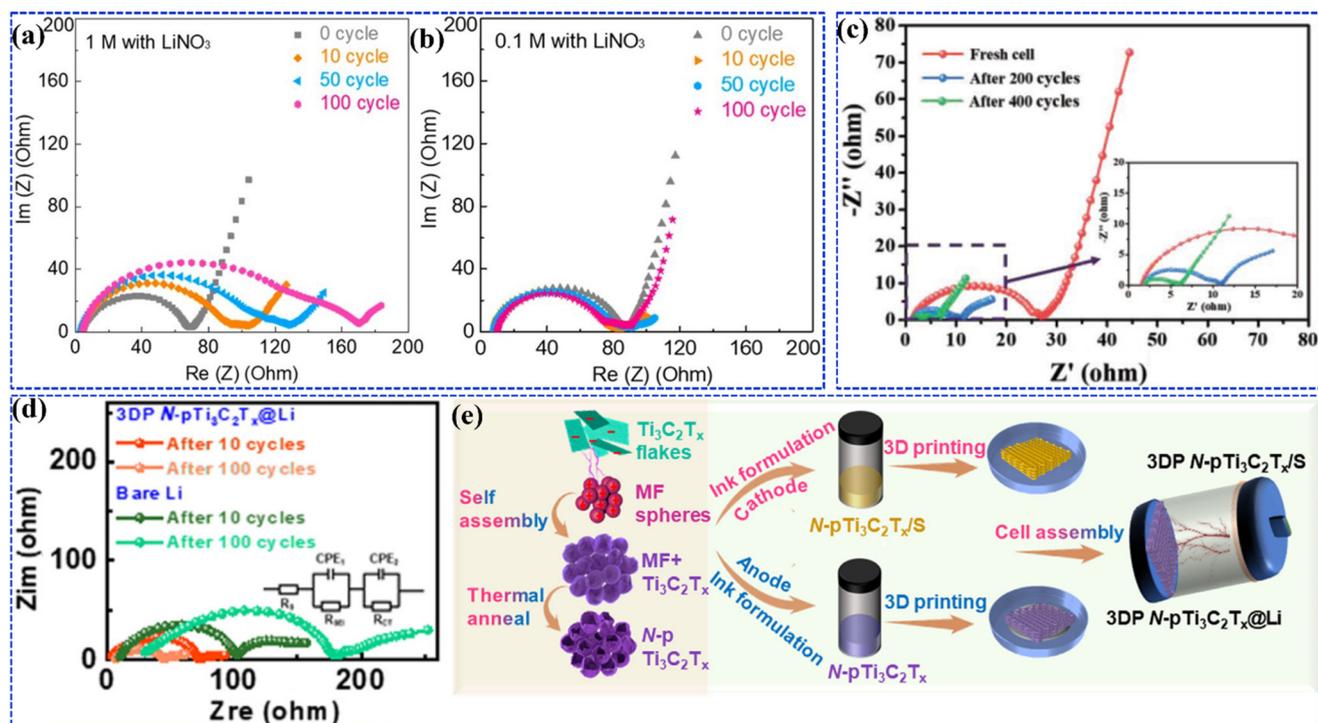
Fig. 1 EIS variations in cells over 100 cycles in (a) 1 M and (b) 0.1 M electrolytes; reproduced with permission.[50] Copyright 2020, American Chemical Society. (c) EIS plot of the integrated S-CNTs/Concan's/PVDF membrane after 200 and 400 cycles; reproduced with permission.[51] Copyright 2019, Wiley-VCH. (d) EIS plots of Li symmetric cells after 10 and 100 cycles and (e) schematic of LiSB preparation using a 3D-printed N-pTi₃C₂Tₓ framework. Reproduced with permission.[52] Copyright 2021, Elsevier.
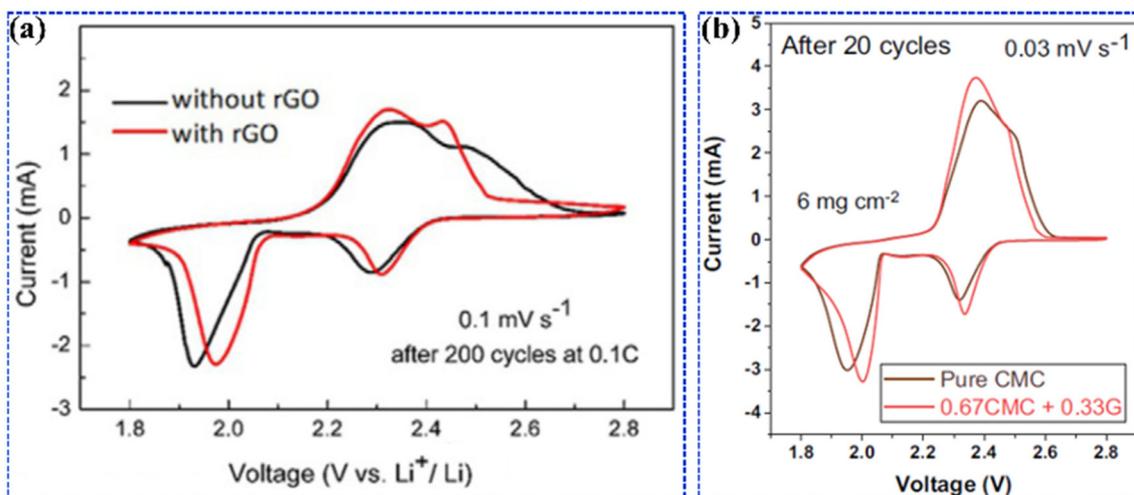
Fig. 2 (a) CV profiles of LiSBs with and without rGO after 200 cycles at 0.1 C; reproduced with permission.[57] Copyright 2018, Wiley-VCH. (b) CV profiles of different cathodes. Reproduced with permission.[58] Copyright 2021, Springer Nature.

system occurred at higher voltage ranges compared to the CMC cathode, reflecting lower electrochemical reaction resistance.

3.2. Microscopic techniques

Microscopy is pivotal in the post-mortem analysis of LiSBs, offering detailed insights into the structural and morphological alterations occurring during cycling.[62] Techniques such as electron and optical microscopy enable the examination of electrode morphology, sulfur species distribution, and SEI layer formation.[63,64] This detailed microscopic analysis is crucial for elucidating the degradation mechanisms responsible for capacity loss and cycling instability in LiSBs.[64] Key microscopic methods include:

3.2.1 Scanning electron microscopy (SEM). SEM when used in post-mortem analysis of LiSBs, offers detailed insights into the surface morphology and structural changes of the cell components, including electrodes, separators, and other elements.[65] This technique enables high-resolution imaging, facilitating the identification of key features such as cracking, delamination, and sulfur deposition.[66] These observations provide crucial information about mechanical degradation and electrode–electrolyte interactions, shedding light on the factors contributing to failure.[67] In a classic example by Tian *et al.*,[68] SEM images (Fig. 3a and b) and EDS mapping (Fig. 3c) show uniform loading of 2H/1T MoS$_2$ on N-doped carbon foam (CF) skeletons, which remained intact after 50 charge–discharge cycles. The preserved flexibility and 3D structure of melamine aid in adsorbing and catalyzing LiPSs while buffering volume expansion due to abundant gaps between fragmented structures, resulting in a CF@2H/1T MoS$_2$ interlayer battery with excellent cycling stability (0.049% decay at 2 C). In another study, Song *et al.*[69] used a dual-template method to create porous carbon spheres (PNCS) with high porosity and specific surface area, which maintained a smooth

lithium metal anode surface after 50 cycles, as shown in SEM images (Fig. 3d and e). The cathode's porosity, high sulfur loading, extensive cathode/electrolyte interaction, and open pore channels contributed to an initial discharge capacity of 1445 mA h g^{-1} at 0.2 C and a minimal capacity decay of 0.047% per cycle.

Conducting polymers like polyaniline, known for their strong LiPS affinity and high conductivity, face challenges such as low polarity, instability, and limited surface area.[74,75] To address these issues, Chen *et al.*[70] developed a stable and 3D microporous conjugated microporous polyaniline (CMPA) with an extended p-conjugated system by combining the high surface area and N-rich properties of microporous polymers with the stability and conductivity of polyaniline. SEM analysis of cathodes post 200 cycles (Fig. 3f–h) reveals amorphous agglomerates of sulfur-modified materials and fused CNFs, leading to the collapse of the 3D CNF/S network. The optical image of the lithium anode (Fig. 3i) paired with the CNF/CMPA/S cathode shows minimal polysulfide presence, highlighting CMPA's superior LiPS trapping capability, which contributes to a high areal capacity of 7.42 mA h cm^{-2} and an energy density of 202.8 W h kg^{-1} cell, even at a sulfur loading of 8.72 mg cm^{-2}.

The mixed-metal spinel oxide Co$_2$Mn$_{0.5}$Al$_{0.5}$O$_4$ (CMA) is an effective cathode material,[76] with its cobalt and manganese oxides strongly interacting with sulfur species and its spinel structure—featuring tetrahedral and octahedral vacancies—actively trapping polysulfides and various LPS species. Santos *et al.*[71] created a carbon-CMA composite for LiSBs, which showed folding-fan-like structures in SEM images (Fig. 3(j–l)), indicating effective LiPS trapping. The 90% CMA electrode (Fig. 3(m–o)) exhibited no needle-like structures, suggesting different SEI properties and demonstrating CMA's superior LiPS trapping, enhancing initial capacity to 1000 mA h g^{-1} and extending cyclability to about 360 cycles. In a significant study

Fig. 3 SEM images and EDS spectra of CF@2H/1T MoS$_2$, (a) before cycling, (b and c) after 50 cycles; reproduced with permission.[68] Copyright 2021, American Chemical Society. Surface mor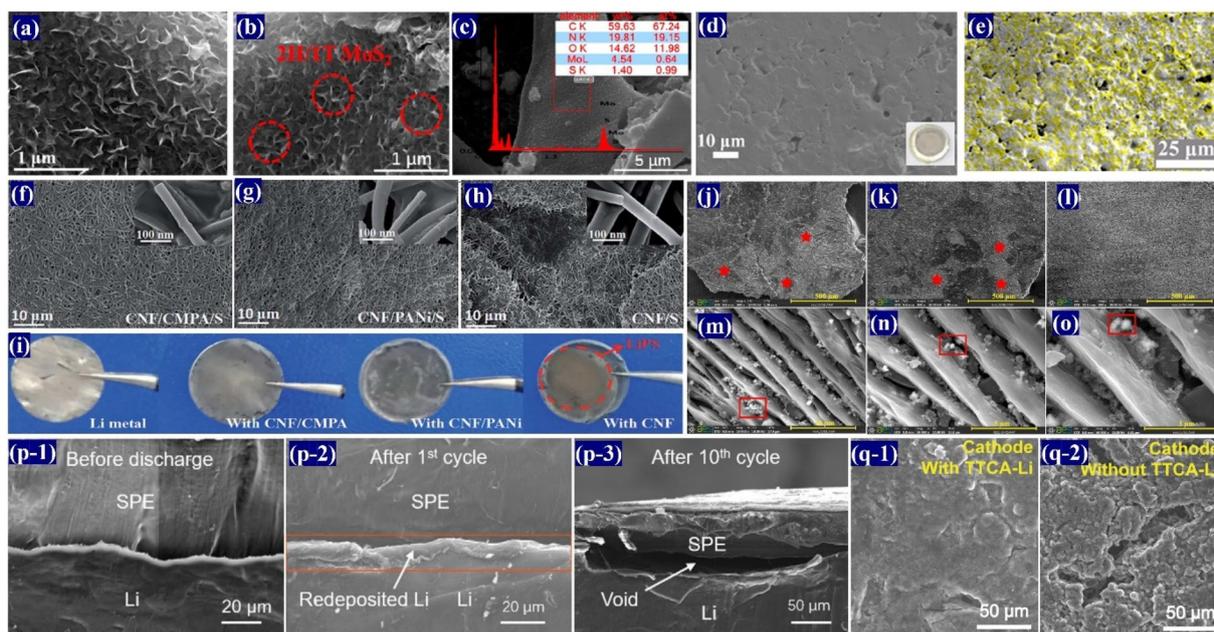phology of lithium metal anodes (d) before cycling and (e) after cycling, from the Li–S batteries using S@PNCS/NG cathode over 50 cycles at 1 C. Reproduced with permission.[69] Copyright 2022, American Chemical Society. SEM image after 200 cycles for (f) CNF/CMPA/S (g) CNF/PANi/S, (h) CNF/S electrode (i) optical image of the fresh and cycled lithium. Reproduced with permission.[70] Copyright 2022, Royal Society of Chemistry. (j–l) SEM images of electrodes containing different CMA contents and (m–o) folding fan structure. Reproduced with permission.[71] Copyright 2023, Elsevier. (p) Cross-section SEM image of the Li anode-SPE interface in the S/SPE/Li cell (p-1) before discharge, (p-2) after the first cycle, (p-3) after ten cycles. Reproduced with permission.[72] Copyright 2021, Wiley-VCH. (q) SEM images of Li$_2$S cathodes after 5 cycles in electrolytes with/without TTCA-Li. Reproduced with permission.[73] Copyright 2023, Wiley-VCH.

by Liu and colleagues,[72] liquid electrolyte-based lithium–sulfur batteries (LELS) were shown to outperform solid electrolyte-based batteries. In LELS systems, only soluble polysulfides dissolve into the electrolyte and induce uniform corrosion of the anode. In contrast, in solid-state batteries using a PEO-based solid electrolyte, both polysulfides and sulfur dissolve, leading to uneven passivation on the anode surface. This uneven passivation results in non-uniform Li$^+$ plating and stripping at the anode/solid electrolyte (SPE) interface (Fig. 3p). Over successive charge–discharge cycles, this inhomogeneity worsens, causing fluctuations in overpotential and ultimately resulting in cell failure. Similarly, Geng _et al._[73] developed a Li$_2$S cathode coated _in situ_ with a polymerizable electrolyte additive, trithiocyanuric acid trilithium salt (TTCA-Li), to reduce initial overpotential and limit lithium polysulfide shuttling. A full cell featuring the coated Li$_2$S cathode paired with a lithium anode demonstrated coulombic efficiency exceeding 99.5%. The approach also proved effective in lithium-free cells, as shown in a high Li$_2$S-loading pouch cell, and was extended to sulfur-based batteries using TTCA-Li additives. The SEM images (Fig. 3q) after five cycles revealed that the TTCA-Li-coated Li$_2$S cathode maintained a smooth and stable surface, while the uncoated Li$_2$S cathode exhibited significant surface roughness and structural fracture due to sulfur redistribution during cycling.

3.2.2 Transmission electron microscopy (TEM). TEM provides detailed insights into structural and chemical changes in cycled LiSBs, revealing shifts in morphology and distribution of active materials, which are critical for evaluating battery performance. Additionally, TEM detects degradation products, such as SEI layers, and examines their impact on battery performance, providing valuable information on mechanisms behind capacity fade and impedance increase.[77–81] Using a carbonate electrolyte, Pai _et al._ engineered a γ-sulfur phase composite on carbon nanofibers (CNFs) for LiSBs, achieving notable reversible capacity and extended cycle life.[82] TEM images (Fig. 4a-1) demonstrate sulfur particles adhering to CNFs after 1000 cycles, while HRTEM (Fig. 4a-2) confirms the formation of Li$_2$S with a 3.30 Å lattice fringe, indicative of its cubic phase. This LiSB stabilized at an initial capacity of 800 mA h g^{-1}, exhibited a low decay rate of 0.0375% over 4000 cycles, and retained a capacity of 650 mA h g^{-1} after 4000 cycles. Similarly, Hwang _et al._[83] designed a nanocomposite cathode incorporating sulfur, CNTs and magnesium–aluminum-layered double hydroxides (MgAl-LDH) to improve reaction kinetics and conductivity. TEM/EDX mapping of cathodes cycled for 200 cycles at 1 C in charged and discharged states (Fig. 4b–e) revealed that MgAl-LDH forms stronger bonds with sulfur and LiPSs than CNTs, enabling the battery to achieve an initial capacity of 1375 mA h g^{-1} at 0.1 C, and demonstrate
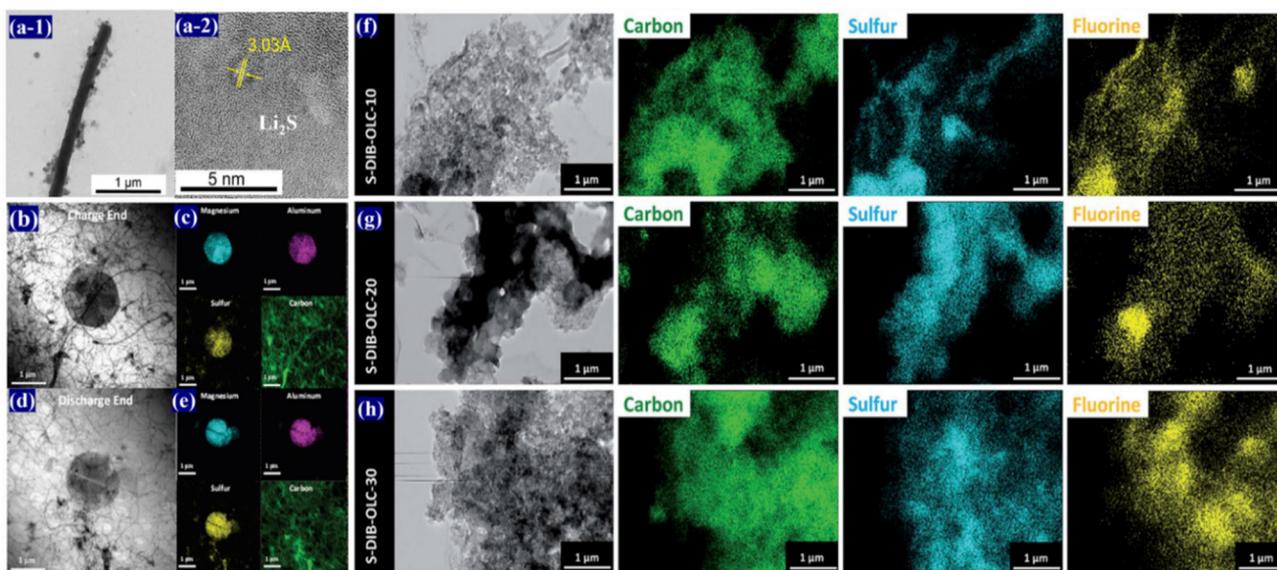
Fig. 4 (a-1) TEM image after 1000 cycles, (a-2) HRTEM image after discharging. Reproduced with permission.[82] Copyright 2022, Springer Nature. TEM and EDX mapping of cathode after 200 cycles at 1 C (b and c) charged state and (d and e) discharged state; reproduced with permission.[83] Copyright 2018, Wiley-VCH. TEM of the electrodes after 100 cycles and corresponding EDX mapping for (f) S-DIB-OLC-10; (g) S-DIB-OLC-10; (h) S-DIB-OLC-30. Reproduced with permission.[84] Copyright 2017, Royal Society of Chemistry.

high-rate capability up to 5 C with a sulfur loading of 4.0 mg cm^{-2}. In a separate study, Choudhury et al.[84] synthesized a sulfur–1,3-di-isopropenylbenzene copolymer via ring-opening radical polymerization, hybridized it with carbon onions at various loadings, and mixed the softened copolymer with carbon onions using a two-roll mill to preserve nanostructures. TEM-EDX analysis after 100 cycles (Fig. 4f–h) showed uniform material distribution, with the initial capacity of 115 mA h g^{-1} in LiSBs increasing to 790 mA h g^{-1} after 140 cycles.

3.2.3 Atomic force microscopy (AFM). AFM can examine electrode topography and morphology before and after cycling, providing insights into changes like surface roughness, cracking, and surface film formation, and identifying degradation mechanisms and failure modes in the battery materials.[85,86] AFM probes mechanical properties such as stiffness and adhesion, revealing material integrity and mechanical stresses.[87,88] Combining AFM with electron microscopy and spectroscopy provides a comprehensive understanding of structural and mechanical changes in cycled batteries.[89]

The formation of inhomogeneous lithium deposition and rough SEI layers in lithium anodes leads to dendritic growth and the accumulation of "dead lithium", resulting in reduced efficiency, capacity fading, and safety risks.[90,91] Senthil et al. used AFM to analyze lithium anodes after 800 hours of cycling,[92] finding that bare lithium anodes exhibited insufficient elasticity to accommodate strain during lithium expansion, as indicated by cantilever tip deflection (Fig. 5a). In contrast, graphene quantum dot (GQD)-modified anodes showed a more linear deflection pattern, suggesting elastic SEI restructuring, a smoother surface, and enhanced cycling stability (Fig. 5b). The lithium anode was recovered from an in situ restructured graphene quantum dots (GQDs) based separator,

which not only formed an ultrasmooth and thin SEI by creating an intimate microstructure with the metallic lithium but also served as a physical barrier to prevent polysulfide diffusion and shuttle effects, thus reducing polysulfide deposition and lithium metal corrosion. To enhance SEI formation, Wang et al.[93] developed a symmetrical polypropylene separator modified on both sides with VS$_2$ nanotowers to maintain pore integrity. AFM images after 100 cycles (Fig. 5c) showed that while a standard PP separator developed rough dendritic surfaces, the VS$_2$-modified separator remained smooth and effectively prevented dendrite growth. This separator exhibited a 16-fold increase in capacity (8.3 mA h cm^{-2}) compared to a conventional PP separator (0.5 mA h cm^{-2}) due to its "sulfiphilic" and "lithiophilic" properties, which mitigate LiPSs shuttle and support stable lithium growth.

3.2.4 Optical imaging. This is a convenient and effective method to document physical changes in cycled batteries.[94] High-resolution images of electrodes, separators, and other components before and after cycling allow visual comparison of morphological changes during battery operation.[95] These images reveal details like cracking, delamination, and surface morphology changes, providing insights into degradation mechanisms and failure modes.[96] Additionally, optical imaging documents the battery's assembly and disassembly, visually recording any damage or wear during handling, aiding in identifying potential degradation sources and developing mitigation strategies.[94]

In a notable example, Zeng et al.[97] developed a metal–organic framework (MOF)-sulfur copolymer cathode to enhance redox kinetics and Li-ion transfer efficiency. After 100 cycles at a rate of 1 C, the CNT@UiO-66-V/S cathode exhibited the presence of notable yellow polysulfides (Fig. 6a) and cor-
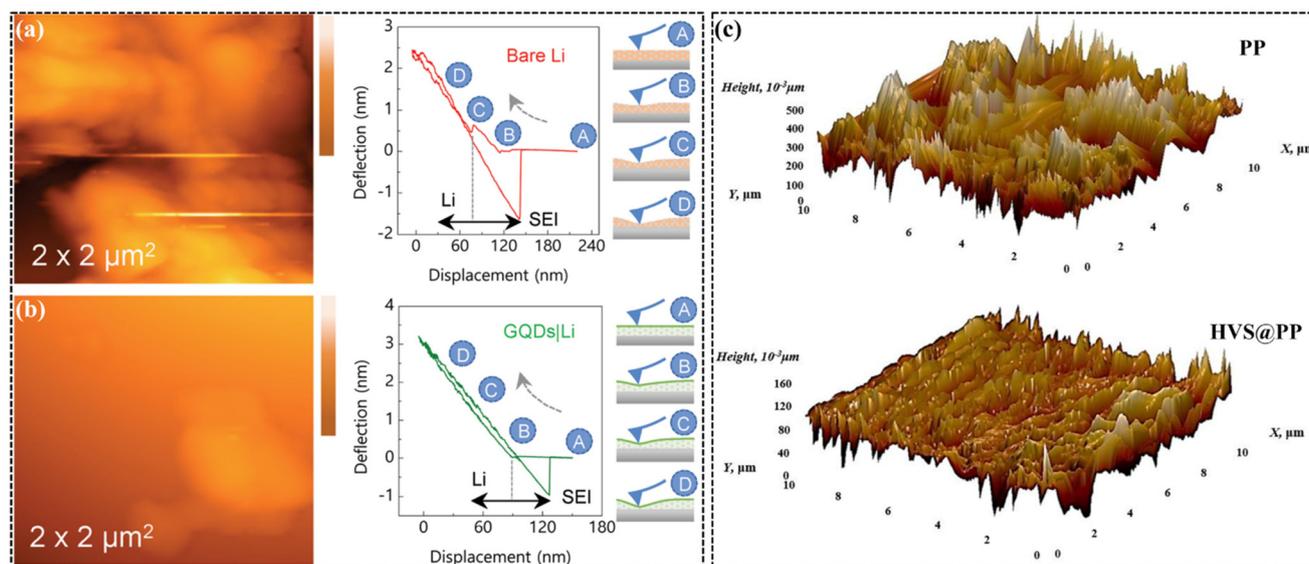
Fig. 5 Images of Li anodes recovered from bare Li (a) and GQDs employed cell (b); reproduced with permission.[92] Copyright 2022, Wiley–VCH. (c) AFM images of the surfaces of the lithium anode in the symmetric cells with different separators after 100 cycles. Reproduced with permission.[93] Copyright 2020, American Chemical Society.

roded lithium metal anode, while the CNT@UiO-66-V-S anode (Fig. 6b) maintained a smoother surface with thinner dendrites and showed no detectable LiPSs. The CNT@UiO-66-V-S cathode delivered over a 100% improvement in discharge capacity at high sulfur loadings, demonstrating its superior electrochemical performance. In another study, Cheng et al.[98] investigated 2D transition metal disulfides (VS_2 and NbS_2), finding that VS_2 adsorbed polysulfides slightly better, enhancing catalytic activity. Incorporating 1/3 V into NbS_2 slabs to form Nb_3VS_6 yielded high capacities of 1541 mA h g^{-1} at 0.1 C and retained 73.2% capacity post 1000 cycles. Optical images (Fig. 6c–f) showed that polyethylene separators with Nb_3VS_6 effectively suppressed shuttling and remained almost pristine.

In another work, Carriazo et al.[99] demonstrated the effectiveness of innovative porous carbon composites for sulfur cathodes by synthesizing two distinct types: one combining graphene oxide (GO) with coffee waste-derived carbon (rGOCaf) and another formed through resorcinol/formaldehyde condensation with GO (ResFArGO), with both composites characterized by the incorporation of graphene and small micropores, which together enhance electronic conductivity and efficiently trap LiPS. The LiSB with ResFArGO achieved over 1100 mA h g^{-1} capacity at high sulfur loadings (4 mg cm^{-2}) and excellent C-rate performance. Post-mortem analysis (Fig. 6g) showed fractured electrodes with detached active material adhering to the separator. Also, Xu et al.[100] developed a flexible MXene-based sulfur cathode featuring V_2C/VO_2 nanoribbons (V_{COR}) pillared between V_2C/VO_2 nanosheets (V_{COS}) during hydrothermal processing, creating a robust, lightweight sandwich architecture. Post-mortem analysis (Fig. 6h) revealed a clean, smooth surface on the separator and Li foil, indicating effective LiPS blocking by the V_2C-160 host which enables the

cell to realize a high areal capacity of 6.3 mA h cm^{-2} and exceptional capacity holding under bending conditions.

3.3. X-ray-based spectroscopic techniques

X-ray-based spectroscopic techniques are crucial for analyzing cycled batteries, offering detailed insights into their chemical composition, structural evolution, and surface chemistry.[101–103] These methods enable the assessment of oxidation state changes, formation of the SEI layer, and surface reactions during battery operation. Additionally, they track alterations in crystal structure and phase composition, providing a deeper understanding of degradation mechanisms and failure modes in battery materials.

3.3.1 X-ray photoelectron spectroscopy (XPS). XPS is a valuable tool for analyzing cycled batteries, providing detailed insights into the chemical composition and electronic states of electrode materials by detecting changes in elemental concentrations, identifying reaction products such as lithium sulfides or oxide layers that indicate degradation mechanisms.[104,105] Additionally, XPS examines the shifts in oxidation states to reveal the extent of electrochemical reactions during cycling, with higher oxidation states of transition metals post-cycling often suggesting side reactions with the electrolyte, thus elucidating battery degradation processes.[106,107] XPS also provides information on the chemical bonding environment of elements in electrode materials, offering insights into SEI layer formation critical for battery performance.[108] XPS depth profiling studies elements and chemical species distribution within electrode materials. Sputtering the surface and analyzing XPS spectra at different depths reveals depth-dependent composition and oxidation state changes, providing insights into battery cycling pro-
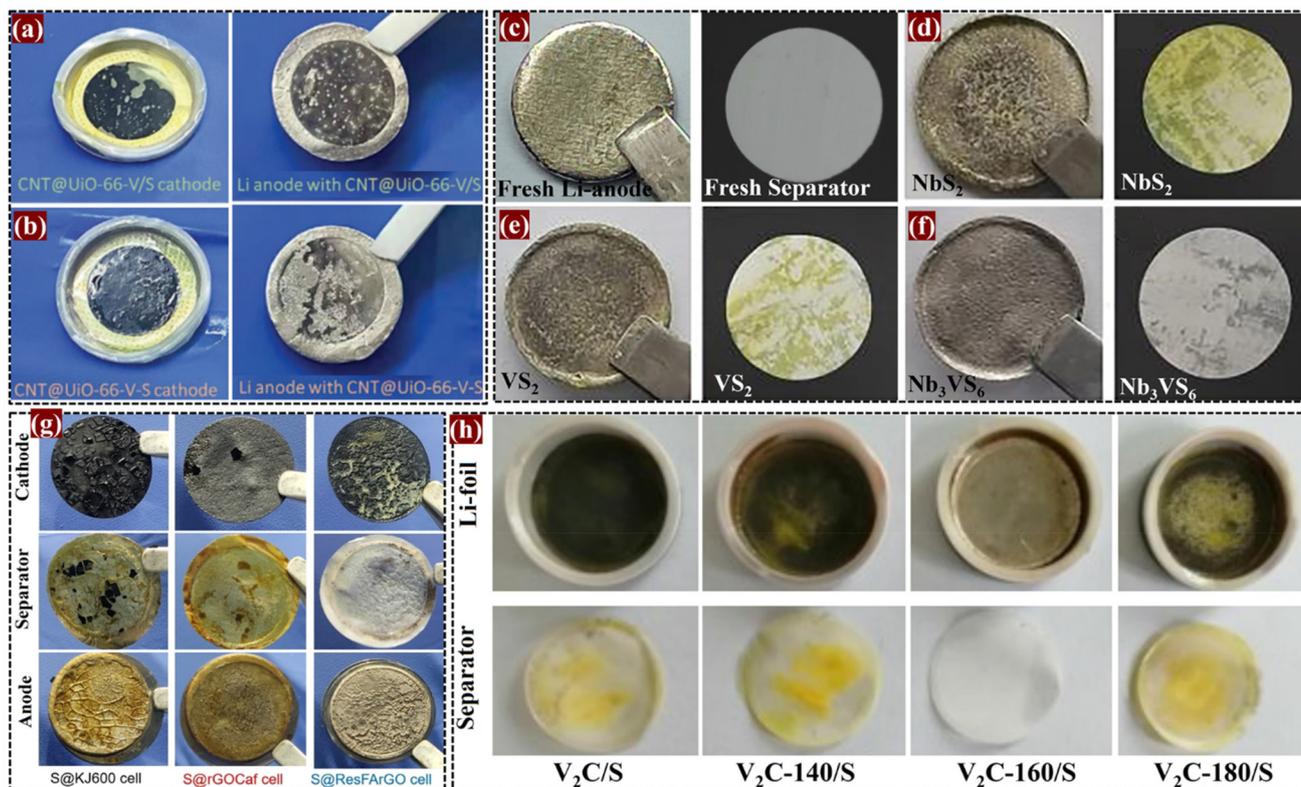
Fig. 6 (a and b) Digital images of battery with different cathodes after 100 cycles; reproduced with permission.[97] Copyright 2022, Wiley-VCH. (c) Optical images of Li metal and separator before cycling, post-mortem analyses of the (d) NbS_2, (e) VS_2, and (f) Nb_3VS_6 cells after 200 cycles at 1 C; reproduced with permission.[98] Copyright 2023, American Chemical Society. (g) Optical images of the cathode, separator, and anode of the S@ResFArGO based pouch cell after cycling; reproduced with permission.[99] Copyright 2022, Wiley-VCH. (h) Photographs of the anodes and separators of the V_2C/S, V_2C-140/S, V_2C-160/S and V_2C-180/S cells (from left to right) after 500 cycles at 0.5 C. Reproduced with permission.[100] Copyright 2021, Royal Society of Chemistry.

cesses.[109] This capability is valuable for studying SEI layer formation and evolution, as well as lithium-ion diffusion into electrode materials.[105,107]

Du et al.[110] employed XPS to investigate a polyethylene (PE)-supported gel polymer electrolyte (GPE) incorporating ester-rich pentaerythritol tetraacrylate (PETEA) and divinyladipate, which achieved an ionic conductivity of 2.8×10^{-4} S cm^{-1}. XPS analysis after 100 cycles (Fig. 7a) revealed the disappearance of the C=O peak (288.7 eV) from the polymer matrix, indicating interaction with lithium polysulfides (LiPSs). This interaction contributed to the battery's ability to retain 70% of its capacity after 300 cycles at 0.5 C, a significant improvement over the 29% retention observed with a liquid electrolyte, highlighting the effectiveness of the ester groups in capturing polysulfides and enhancing cycling stability.

Carbon-based nanofibers, with high electrical conductivity, enhance Li storage in materials like hard carbon and graphite but often have lower Li affinity than metal oxides (e.g., ZnO, Al_2O_3, SiO_2, TiO_2), and metals (e.g., Ag, Si, Mg) with lower Li nucleation barriers.[114,115] To address this, Wang et al. developed TiO_2/SiO_2 (A-TS) nanofiber membrane which promotes uniform charge distribution and fast Li$^+$ diffusion.[111] The XPS spectra of the cycled cell (Fig. 7b) provided critical insights

into the electrochemical conversion and alloying processes within the battery, revealing the presence of various Li-containing compounds, including SiO_2 (with peaks at 103.0 and 102.1 eV), Li_4SiO_x (at 101.1 eV), and Li–Si (at 98.1 eV), which indicate successful alloying with "dead" lithium. Additionally, the presence of a Li–F bond at 55.7 eV suggests the formation of the SEI layer or possible interactions between "dead" lithium and the electrolyte, further elucidating the chemical transformations occurring during cycling.[40]

Further to enhance SEI protection in LiSBs, Pathak et al.[112] developed a worm-like sulfur-polypyrrole (S-PPy) cathode. This core–shell structure prevents polysulfide–electrolyte contact, reducing capacity fading and improving sulfur utilization. XPS analysis of cycled cells (Fig. 7c and d) reveals Li–S, Li_2Se, and Li_2S_x species at B.E. < 163 eV and SEI layer S–O species at B.E. > 164 eV. The Li 1s peak at 53.6 eV indicates a strong interaction between LiPS and the polymer matrix. Also, Wang et al. developed flexible, high-flux electrospun fibrous membranes that improve LiPSs trapping, electron transfer, and Li-ion diffusion.[51] XPS analysis (Fig. 7e) revealed key insights into the chemical processes during prolonged cycling of batteries, showing S 2p peaks at 169.1 and 170.2 eV that indicate the oxidation of LiPSs to sulfate, likely catalyzed by Co nanoparticles.
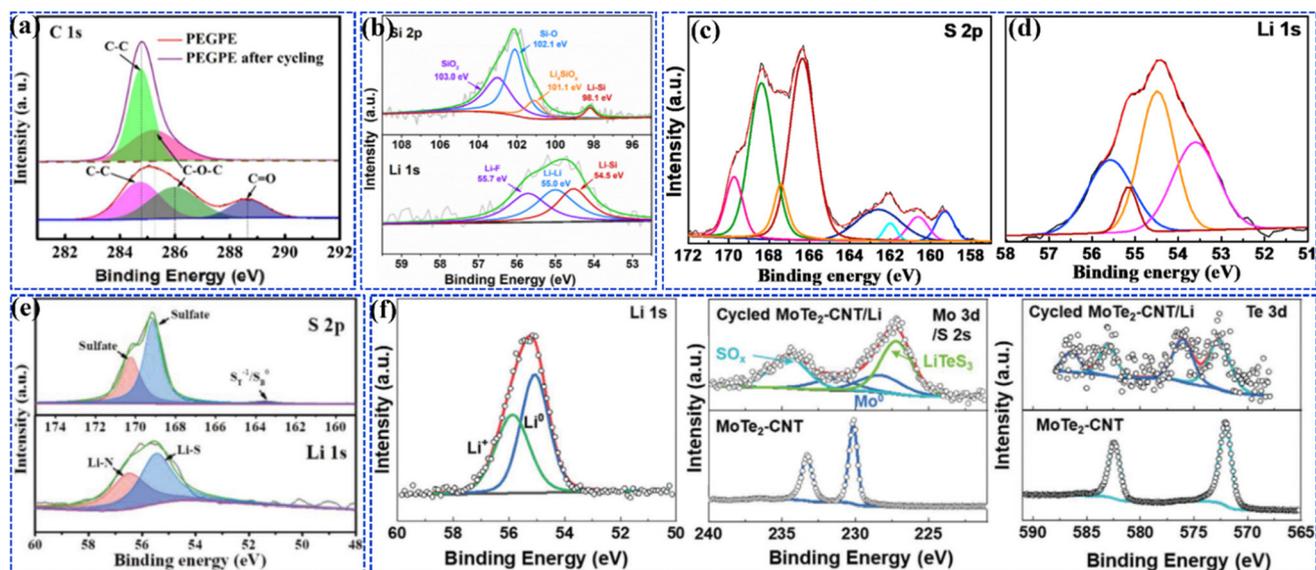
Fig. 7 (a) C 1s XPS spectra of pristine and cycled PEGPE; reproduced with permission.[110] Copyright 2018, Elsevier. (b) XPS spectra of the A-TS membrane after 200 cycles; reproduced with permission.[111] Copyright 2022, Elsevier. XPS spectra of S 2p (c) and Li 1s (d) for the S-PPy electrode cycled in a ternary electrolyte; reproduced with permission.[112] Copyright 2021, Elsevier. (e) XPS spectra of S 2p and Li 1s after 400 cycles; reproduced with permission.[51] Copyright 2019, Wiley-VCH. (f) XPS spectra of Li 1s, Mo 3d, and Te 3d regions after 50 cycles. Reproduced with permission.[113] Copyright 2022, Wiley-VCH.

A weak peak at 163–164 eV suggests the presence of terminal and bridge sulfur atoms from newly adsorbed sulfides, while the Li 1s spectrum shows a 56.5 eV peak for Li–N bonds, confirming effective interactions between nitrogen dopants and LiPSs, highlighting the role of CoNCNFs in facilitating redox reactions and stabilizing LiPSs during battery operation. In another work, He *et al.* developed a MoTe$_2$-CNT composite with 1T′-MoTe$_2$ nanosheets that facilitate uniform lithium deposition and generate a thin SEI layer of lithium thiotellurate on the Li surface, stabilizing Li deposition, suppressing electrolyte decomposition, and reducing lithium loss to enhance cycle life.[113] XPS spectra (Fig. 7f) confirmed the presence of a Li$_2$TeS$_3$ coating on the cycled MoTe$_2$-CNT/Li anode, which maintains dense lithium layers, inhibits electrolyte degradation, and minimizes lithium depletion, ultimately extending the battery's operational life.

3.3.2 X-ray diffraction (XRD). XRD is essential for post-mortem analysis of cycled LiSBs, revealing crystal structure, phase composition, and electrode material changes.[116,117] It detects phase transformations and the formation of new phases like lithium sulfides, which are key to understanding degradation and capacity fade. XRD also assesses crystallinity and crystallite size, offering insights into structural evolution and guiding the development of more durable LiSBs.[118,119]

Yeon *et al.*[120] utilized XRD to investigate a nanosulfur (nS) and reduced graphene oxide (rGO) composite, synthesized through spray-frozen assembly and ozonation, which resulted in a robust rGO/nS hybrid that demonstrated enhanced redox kinetics, improved sulfur utilization, and high-rate capacities. Post-mortem XRD analysis after 100 cycles at 0.1 C (Fig. 8a) revealed a prominent peak at 22.8°, associated with the (222)

plane of crystalline sulfur, indicating reversible structural changes in the nS during cycling, with the rGO/nS hybrid achieving a significant capacity of 1269.1 mA h g^{-1}, outperforming other rGO/sulfur hybrids. Yao *et al.* developed a twin-born ultrathin 2D graphene-based mesoporous SnO$_2$/SnSe$_2$ hybrid (G-mSnO$_2$/SnSe$_2$) as a polysulfide inhibitor, combining strong chemical affinity, high conductivity, and a dynamic intercalation–conversion mechanism.[121] XRD patterns after 500 cycles (Fig. 8b) confirmed the stability of the crystalline structure and the reversible intercalation–conversion of SnSe$_2$, maintaining structural integrity during cycling. When used as a separator in LiSBs, this hybrid material enabled high sulfur utilization, achieving 1544 mA h g^{-1} at 0.2 C, with a slow capacity decay rate of 0.0144% over 2000 cycles at 5 C.

Transition metal sulfides (*e.g.* ZnS, SnS, SnS$_2$ *etc.*), known for strong catalytic activity towards LiPSs and high electrical conductivity, hold significant potential in LiSBs, with ZnS demonstrating robust LiPS catalytic ability and SnS offering superior conductivity due to its narrower band gap compared to SnS$_2$.[126,127] Capitalizing on these properties, Yao *et al.*[122] developed a ZnS–SnS heterojunction coated with N-doped carbon shell (ZnS–SnS@NC) as a modification layer on the separator. Post-mortem X-ray diffraction (XRD) analysis (Fig. 8c) revealed that the ZnS–SnS@NC separator preserved its crystalline structure after cycling, indicating its stability and contributing to improved electrochemical performance by facilitating uniform lithium deposition. In a notable advance, metal–organic frameworks (MOFs) have emerged as powerful agents for trapping polysulfides through their chemical affinity with lithium polysulfides (LiPSs). Archana *et al.*[123] demonstrated this potential by employing a ZIF-67-based MOF to
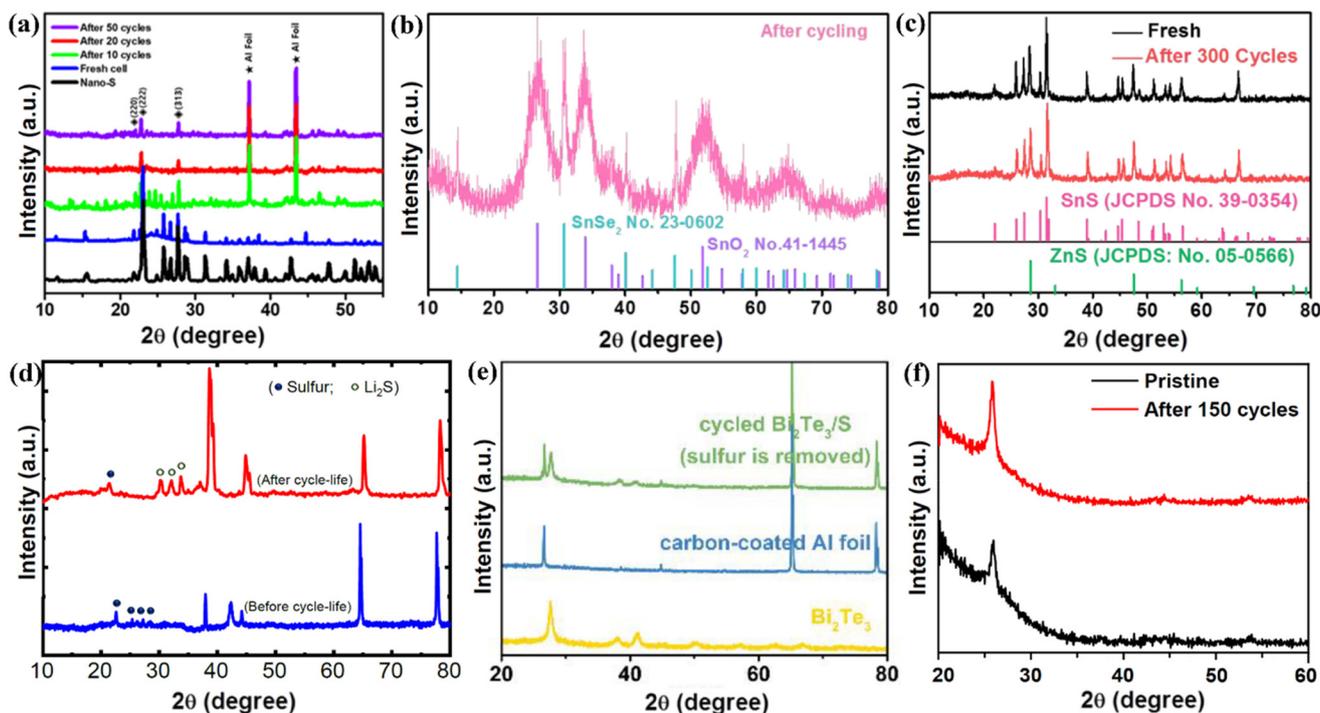
Fig. 8 (a) XRD analysis of fresh and cycled cells; reproduced with permission.[120] Copyright 2019, American Chemical Society. (b) XRD pattern of G-mSnO$_2$/SnSe$_2$ modified separator after 500 cycles at 0.5 C under full charge state; reproduced with permission.[121] Copyright 2022, American Chemical Society. (c) XRD pattern of ZnS-SnS@NC modified separator before and after 300 cycles at 0.2 C; reproduced with permission.[122] Copyright 2021, American Chemical Society. (d) XRD patterns for the ZIF-Co@NCS cathode before and after 600 cycles; reproduced with permission.[123] Copyright 2023, American Chemical Society. (e) XRD pattern of the cycled Bi$_2$Te$_3$/S cathode; Reproduced with permission.[124] Copyright 2022, Wiley-VCH. (f) XRD pattern of the cathode extracted from a cell at the end of 150th charge compared with the pristine electrode. Reproduced with permission.[125] Copyright 2019, American Chemical Society.

engineer a cobalt@nitrogen-doped carbon–sulfur composite (ZIF-Co@NCS) as a cathode host for lithium–sulfur batteries. Post-mortem XRD analysis after 600 cycles (Fig. 8d) unveiled new peaks at 32.1 and 33.7 degrees, corresponding to Li$_2$S, indicative of the discharge product. This finding underscores the remarkable stability and effective Li$^+$ ion storage capabilities of the ZIF-Co@NCS cathode, affirming its role in enhancing battery performance and longevity through robust polysulfide immobilization.

Topological insulators (TIs) like Bi$_2$Te$_3$ are promising for sulfur electrochemistry due to their Dirac cone surface band structure, which offers excellent charge transport properties. Song et al.[124] utilized Bi$_2$Te$_3$, selected for its ultrahigh Hall mobility (10 200 cm^2 V^{-1} s^{-1}) and simple one-step solvothermal preparation, to accelerate sulfur redox kinetics. Bi$_2$Te$_3$ effectively anchored soluble sulfur species, creating seamless electron transport pathways with adsorbed polysulfides. XRD analysis (Fig. 8e) confirmed the crystal structure's stability during cycling, demonstrating Bi$_2$Te$_3$'s ability to enhance both sulfur reduction and reverse reactions. Bhargav et al.[125] synthesized polyethylene hexasulfide (PEHS) via a simple condensation reaction and integrated it into a CNT network to create a composite cathode. Post-mortem XRD analysis after 150 cycles (Fig. 8f) revealed increased intensity of CNT peaks and a lack of distinct sulfur peaks, indicating possible delamination

or inaccessibility of the active material, yet the lithium–sulfur battery still exhibited a high capacity of 1274 mA h g^{-1}.

3.3.3 X-ray absorption near edge spectroscopy (XANES). XANES (Near Edge X-Ray Absorption Fine Structure) is a useful technique to seek details of the chemical and electronic structure of electrode materials by revealing the oxidation states of sulfur species including elemental sulfur, lithium sulfides, and polysulfides, both pre- and post-cycling.[40] This technique distinguishes between various sulfur oxidation states (e.g., S$_0$, S$_2^-$, S$_4^+$), offering crucial information on sulfur utilization and the formation of soluble polysulfides during cycling, which is vital for understanding capacity fade, performance degradation mechanisms, and failure modes in lithium–sulfur batteries.[128,129] Furthermore, XANES can analyze the formation and evolution of the SEI layer, which forms on electrode surfaces and significantly influences battery performance.[130] By studying changes in the XANES spectra of the SEI layer pre- and post-cycling, insights into its chemical composition and stability can be obtained, thus better understanding its impact on battery performance and longevity.[131]

Zubair et al.[132] developed free-standing cathodes by electrodepositing manganese oxide (MnO$_x$) nanoflakes onto carbonized cellulose cloths, which enabled higher sulfur loadings with reduced electrolyte content. They achieved this by surface-engineering the MnO$_x$ nanoflakes through controlled anneal-

ing to obtain various oxidation states, resulting in defective interfaces that enhanced reaction activity, promoted polythionate formation, and improved LiPSs retention on the cathode surface. XANES analysis of the Mn K edge for the cycled electrodes (Fig. 9(a–c)) revealed that the MnO_x/S cathodes processed in air at 300 °C and 400 °C exhibited a decrease in valence, while the MnO_x/S cathode treated in argon at 400 °C showed a shift to a higher oxidation state due to incomplete delithiation, which enhanced structural stability. These

oxygen-deficient manganese oxide nanoflake cathodes maintained a reversible capacity of 824 mA h g^{-1} at 0.5 C over 200 cycles.

In a different approach, Ai[133] *in situ* synthesized CoS_2 nanocrystals within a 3D hierarchical porous graphitic carbon (HPGC), finding that the combination of microporous HPGC's strong physical absorption and polar nano-CoS_2's chemical absorption effectively anchored polysulfides during charge/discharge. *Ex situ* NEXAFS spectra for fresh electrodes (Fig. 9d)
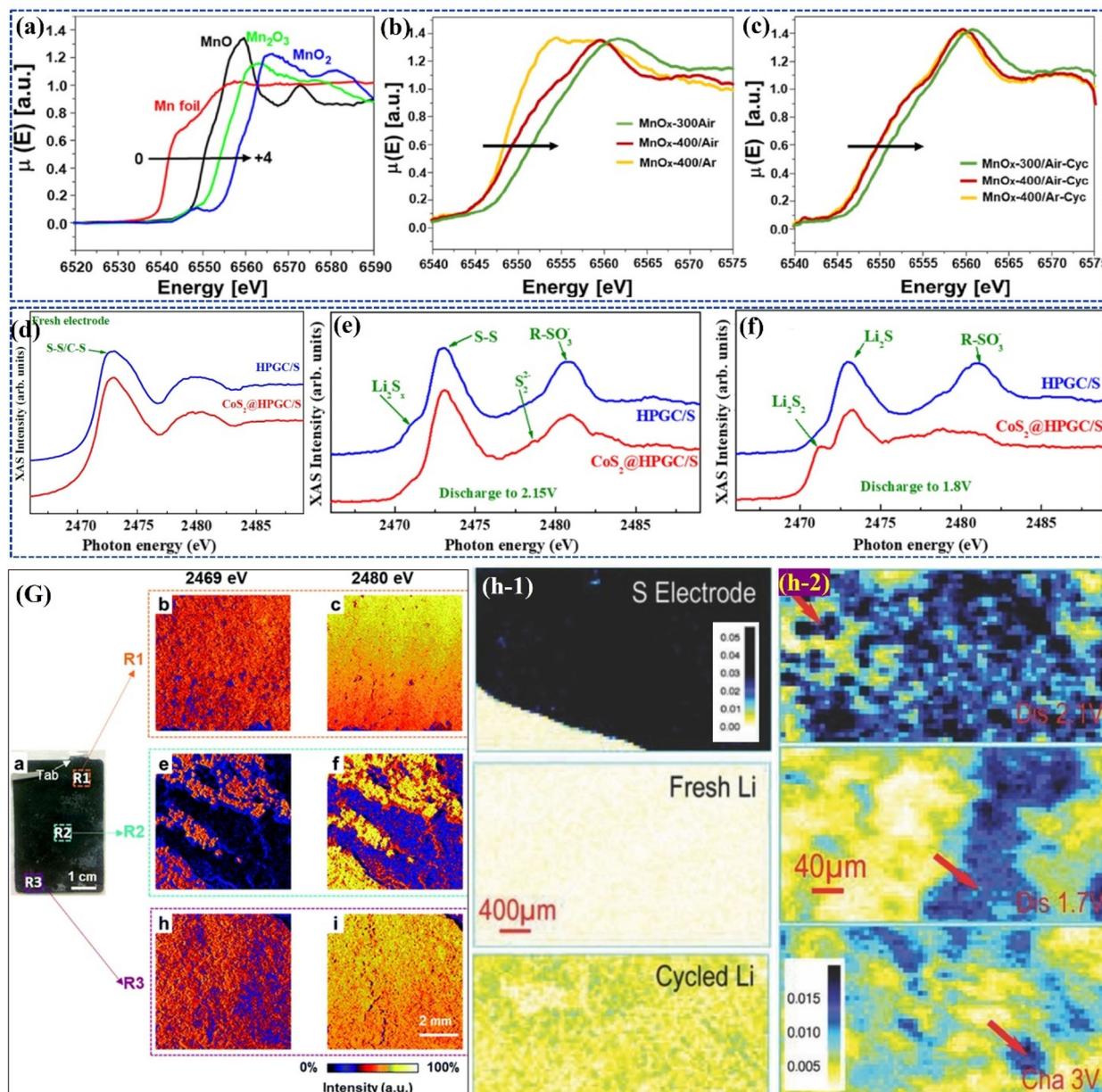
Fig. 9 Mn K-edge XANES spectra for (a) Mn reference compounds, (b) fresh and (c) cycled electrodes. Reproduced with permission.[132] Copyright 2023, Elsevier. TFY-NEXAFS spectra of the S K-edge (d) fresh electrode and cycled electrode discharged to (e) 2.15 V and (f) 1.8 V. Reproduced with permission.[133] Copyright 2019, American Chemical Society. (G) Revealing the local chemical nature of cycled S cathode by combined XRF and XAS analysis. Reproduced with permission.[134] Copyright 2020, Royal Society of Chemistry. (h-1) XRF images collected on sulfur/Ketjen black electrode, fresh Li foil, and cycled Li foil after one cycle,(h-2) XRF images collected on lithium anode electrodes harvested from the Li|Sulfur/Ketjen black cells at discharged 2.1 V, discharged 1.7 V, and re-charged 3 V states. Reproduced with permission.[135] Copyright 2015, Wiley-VCH.

displayed broad peaks around 2473 eV, corresponding to S–S and C–S combinations, and 2480 eV, due to multiple scattering effects and multielectron excitation. Post-cycling analysis of cathodes disassembled at 2.15 and 1.8 V during the first discharge (Fig. 9e and f) revealed similar peaks, with a distinct 2471.0 eV peak indicating differences in polysulfide species, where CoS_2 nanocatalysts enhanced the conversion of LiPSs into short-chain Li_2S_x.

3.3.4 X-ray fluorescence (XRF). XRF is an essential technique for analyzing lithium–sulfur batteries, providing detailed insights into the elemental distribution and composition of battery materials. It enables microscale elemental mapping, crucial for visualizing lithium, sulfur, and transition metals, and understanding key phases like lithium polysulfides.[137] XRF aids in surface characterization by identifying contaminants and degradation products, while its *in situ* analysis capability allows real-time monitoring of elemental changes during charge–discharge cycles, helping to elucidate degradation mechanisms and the evolution of the SEI.[138] In post-mortem analysis, XRF quantifies sulfur content and detects impurities in the cathode, offering insights into sulfur utilization and performance loss. It also maps the spatial distribution of elements, providing valuable information on electrode material homogeneity and reaction byproducts, which are critical for understanding degradation mechanisms and failure modes.[139]

In a classic work by Shi *et al.*[134] on studying the failure mechanism of large-format LiS pouch cells, it was observed that uneven sulfur reactions cause sulfur loss, redistribution, and passivation, leading to morphological and compositional heterogeneities across the cathode. Cycling smooths the electrode surface due to sulfur deposition, while changes in morphology and increased tortuosity may hinder electrolyte flow, ultimately affecting cell performance. XRF imaging of the cycled sulfur cathode (Fig. 9G) reveals that the R1 region is predominantly covered by high-intensity sulfur species, represented in yellow, and randomly distributed low-intensity species in blue. When the cut-off energy is increased to 2480 eV, XRF detects a wider range of sulfur species, confirming uniform coverage in the R1 region. In contrast, the R2 region exhibits significant heterogeneity, as demonstrated by XRF mapping at both 2469 and 2480 eV, indicating more severe heterogeneous reactions. This analysis highlights the presence of varying sulfur oxidation states and different chemical compositions, suggesting that reaction non-uniformity exists across multiple length scales, particularly in the center region compared to the edges. A study by Yu and group[135] suggested that polysulfide dissolution and redeposition lead to sulfur redistribution on the lithium anode, which was further analyzed using *ex situ* XRF on lithium foil anodes (Fig. 9h). The study revealed sulfur species deposited on the anode, contributing to low coulombic efficiency and poor cycle life. Long-chain polysulfides were found on the discharged anode, while insoluble short-chain polysulfides or Li_2S appeared on fully discharged and charged anodes. These findings indicate that polysulfide deposition and anode corrosion significantly contribute to capacity fading in lithium–sulfur batteries, emphasizing the need for anode protection and the development of non-corrosive electrolytes alongside modifications to the sulfur cathode.

Utilizing biocarbon from avocado seeds as a source of activated carbon for LiSBs is a promising approach, especially given that avocado seeds, which account for about 20% of the fruit's weight, are a significant byproduct of the globally consumed 6 million tons of avocados annually, with a 3% growth rate.[140,141] Morales *et al.* employed XRF analysis to derive activated carbon from these seeds and impregnated it with a dual copolymer of polypyrrole and polystyrene sulfonate to enhance electrode performance, particularly at low current densities.[136] Analysis of sulfur content before and after cycling (Table 2) demonstrated that the polymer-impregnated electrode retained a greater amount of sulfur, highlighting its superior ability to absorb polysulfides and suppress the shuttle effect, thereby minimizing irreversible sulfur loss. This improvement led to the LiSB achieving a discharge capacity of approximately 1200 mA h g^{-1} after 250 cycles at 0.1 C.

3.4. Optical spectroscopic techniques

Optical spectroscopic techniques are versatile tools used in batteries for a range of purposes.[142,143] They are employed in the analysis of electrode materials, providing insights into their composition, electronic structure, and properties, aiding in understanding their behavior, and facilitating the development of new materials.[144] Additionally, optical spectroscopy is used to study electrolytes, analyzing their composition, conductivity, and interactions with electrodes, crucial for optimizing formulations and improving battery performance.[145] These techniques also characterize interfaces within batteries, providing information about electrode–electrolyte and electrode–electrode interfaces, essential for enhancing stability and performance. Furthermore, optical spectroscopy not only detects degradation mechanisms like SEI layer formation, material dissolution, and dendrite growth, but also facilitates the development of strategies to mitigate these issues and extend battery lifespan. It also facilitates *in situ* and *operando* studies, enabling live visual and estimation of changes in battery properties during operation, which is crucial for understanding battery behavior and optimizing performance.[146] Following are the important optical spectroscopic techniques reported thus far for LiSBs:

3.4.1 Raman spectroscopy. Raman spectroscopy, which analyzes vibrational, rotational, and other low-frequency modes within a system to provide a distinct molecular fingerprint, offers valuable insights into both chemical composition and structural characteristics.[148] In battery research, it is utilized to assess chemical composition, monitor structural changes such as dendrite formation, and investigate degradation mechanisms in electrodes, electrolytes, and interfaces.[149] Raman spectroscopy plays a crucial role in post-mortem analysis of cycled batteries by examining changes in electrode materials and electrolytes after repeated charge–discharge cycles.[150] It identifies degradation products, such as

Table 2 Sulfur concentrations (in wt%) obtained from XRF and EDS analysis different electrodes before and after cycling. Reproduced with permission.[136] Copyright 2022, Royal Society of Chemistry

XRF technique

Sample	Uncycled	C/10[b]	C/12[c]	1C[b]	2C[b]	5C[b]
ASAC@S	13.4	4.8	6.6	6.7	6.7	7.1
ASAC/PPyPSS@S	14.6	7.2	7.9	8.0	9.3	9.8

EDS technique

| Sample	Uncycled (300×)[a]	Uncycled (1000×)	C/10[b] (300×)	C/10[b] (1000×)	1C[c] (300×)	1C[c] (1000×)
ASAC@S	2.8	4.2	5.4	6.5	7.1	6.6
ASAC/PPy:PSS@S	6.5	6.6	8.5	6.9	10.3	11.7

[a] Magnification of SEM/EDS images. [b] After 250 cycles. [c] After 500 cycles.

lithium compounds and polysulfides, offering valuable insights into capacity fade and performance decline. Additionally, Raman spectroscopy detects structural changes in electrode materials, including phase transformations and mechanical degradation, which are essential for designing more durable and efficient battery systems.[151]

Organosulfur compounds like sulfurized-polyacrylonitrile (SPAN) have gained attention for LiSBs due to their sustainability and lightweight properties, though their application is limited by low sulfur content, typically below 50 wt%.[152] To address this, Weret et al. synthesized a fibrous sulfurized trithiocyanuric acid/polyacrylonitrile (STTCA@SPAN) composite via electrospinning TTCA with PAN, followed by inverse vulcanization, which leveraged TTCA's highly oxidizable thiol groups to increase the sulfur content to 58 wt%.[147] The resulting fibrous cathodes achieved an initial discharge capacity of 1301 mA h g^{-1} and exhibited excellent cycling stability over 400 cycles, demonstrating the effectiveness of this approach in enhancing LiSB performance. The post-mortem analysis in Fig. 10a and b demonstrates that the cross-linked fibrous structure of the STTCA@SPAN cathode maintains its stability

throughout extended charge–discharge cycles, as evidenced by the preservation of structural integrity. Ex situ Raman spectroscopy of the cycled cathodes in Fig. 10c reveals that while the intensities of the S–S, C–S, and S–N peaks diminish after complete discharge, they reappear upon full charging, indicating the reversibility of the electrochemical redox reactions, with a decrease in the ID/IG intensity ratio post-cycling further suggesting the involvement of conjugated C=N and C=C bonds in lithium storage. In another work, Santos et al.[71] developed a spinel oxide $Co_2Mn_{0.5}Al_{0.5}O_4$ (CMA), demonstrating impressive performance in LiSBs with an initial capacity of 1000 mA h g^{-1} cm^{-2} and enhanced cyclability beyond 360 cycles. The Raman spectrum of the 50% CMA electrode (Fig. 10d), shows significant structural changes pre- and post-cycling, including the shift of elemental sulfur peaks and the emergence of a new peak at 609 cm^{-1}, attributed to the M–O stretch mode of $LiMO_2$ (M = Mn or Co), indicating that lithiation and redox mediator behavior critically contribute to CMA's superior performance in LiSBs.

3.4.2 Fourier transform infra-red (FTIR) spectroscopy. FTIR spectroscopy investigates the chemical composition and struc-
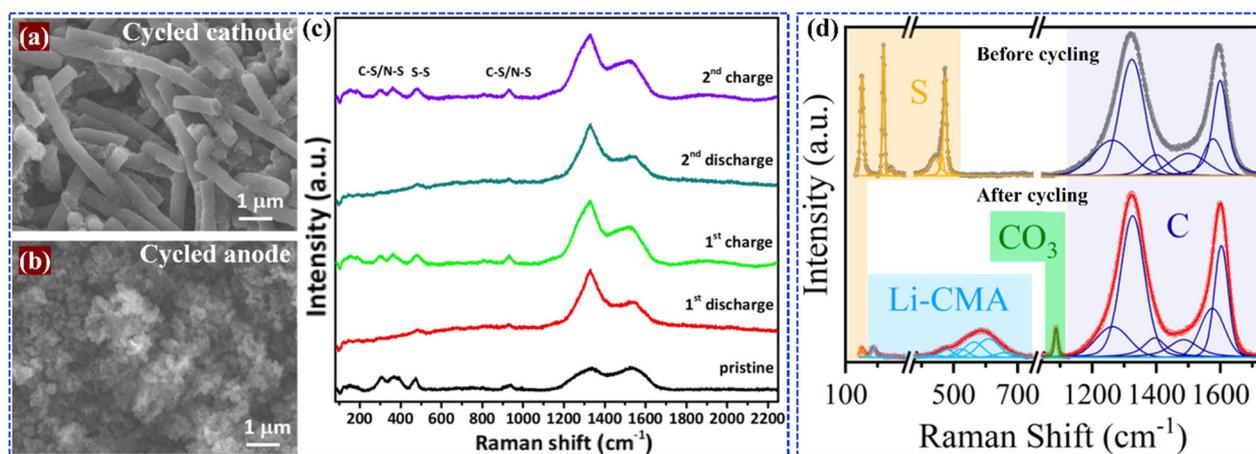
Fig. 10 The SEM images include the cycled cathode (a), the cycled Li anode (b), and Raman spectra of cathode (c); reproduced with permission.[147] Copyright 2022, Elsevier. (d) Raman spectra of 50% CMA electrodes. Reproduced with permission.[71] Copyright 2023, American Chemical Society.

ture of materials by passing infrared light through a sample and recording the resulting spectrum of absorbed or emitted light.[153] This spectrum provides insights into functional groups, chemical bonds, and other molecular properties, allowing for detailed analysis of the material's structure.[71] In battery research, FTIR serves as an indispensable tool for characterizing the SEI layer by providing insights into its composition, thickness, and formation mechanisms, which are critical for optimizing battery performance, while the analysis of FTIR spectra allows researchers to identify and quantify impurities and degradation products within electrolytes, informing the refinement of electrolyte formulations for enhanced performance and stability.[154] Furthermore, FTIR spectroscopy serves as a valuable tool for investigating degradation processes in electrode materials, including the formation of lithium dendrites and the decomposition of active materials, providing crucial insights into the factors limiting battery longevity and performance.

Dillard et al.[155] utilized FTIR post-mortem analysis to examine sulfur deposition onto electrospun carbon nanofibers (CNF), resulting in a binder-free, freestanding cathode that bypasses the need for slurry processing, insulating binders, toxic solvents, and heavy current collectors. The FTIR analysis of the S-CNF cathode (Fig. 11a) revealed a redshift in bands between 3100 and 600 cm^{-1}, indicating weakened bonds within the CNF surface functional groups due to interactions with polysulfides (Table 3). This redshift suggests that polysulfides chemisorbed onto the CNF surface form covalent or weaker van der Waals/hydrogen bonds, redistributing electrons at 'binding sites' such as nitrogen or oxygen functionalities and leading to the weakening or stretching of local bonds; for instance, polysulfides interacting with pyridinic nitrogen cause adjacent C–N bonds to weaken as the nitrogen moves towards the polysulfide. In a notable study, Du et al.[156] developed a polyethylene-supported gel polymer electrolyte (GPE) with ester groups by cross-linking pentaerythritol tetraacrylate (PETEA) with divinyladipate, and post-mortem FTIR analysis (Fig. 11b)

Table 3 Summary of absorption frequency redshift in the 3400–400 cm^{-1} region of the FT-IR spectra of reference and post-mortem S-CNF samples corresponding to the starred peaks in Fig. 11. Reproduced with permission.[155] Copyright 2018, Elsevier

Assignment	Pristine CNF	Soaked S-CNF	Cycled S-CNF
N–H$_2$ stretch	3325	3489	3203
CH/CH$_3$ stretching	2954	2947	2943
CH/CH$_3$ stretching	2917	2917	2912
CH/CH$_3$ stretching	2848	2846	2842
C=O in quinine or conjugated ketone group	—	1635	1621
C–C/C–H bending	1455	1456	1455
C–H loop bending in aromatic carbon	788	768	767

revealed that the C=O stretching peak at 1739 cm^{-1} nearly vanished after 100 cycles, indicating significant chemical changes. This PEGPE demonstrated retained 70% of its capacity after 300 cycles at 0.5 C, compared to just 29% with a liquid electrolyte, due to the ester groups' ability to trap polysulfides and the optimized SEI film on the Li metal anode.

3.4.3 Inductively coupled plasma-atomic emission spectroscopy (ICP-AES). ICP-AES is a pivotal technique for both qualitative and quantitative elemental analysis, utilizing an ICP as a high-temperature ionization source to atomize and excite the elements within a sample, thereby enabling precise determination of their concentration and distribution.[158] In battery research, ICP-AES is essential for post-mortem analysis of cycled cells, specifically for examining the elemental composition of battery materials and electrolytes. It measures the concentration and distribution of trace metals such as lithium and carbon, offering insights into material uniformity and cycling behavior.[159] Additionally, ICP-AES is used to assess changes in the elemental composition of electrode materials and electrolytes after cycling, which helps in understanding their effects on battery performance and longevity. Wang
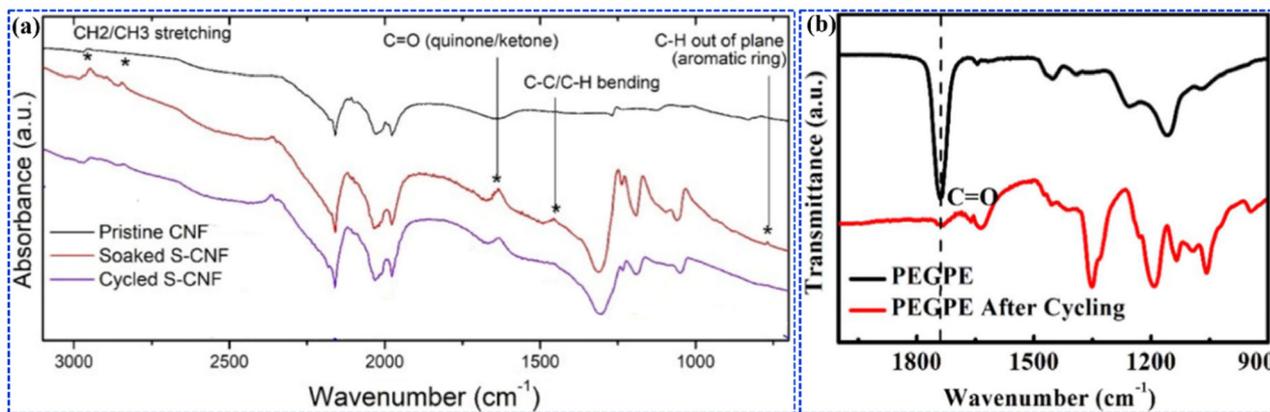
Fig. 11 (a) FT-IR absorption spectra of reference CNF, S-CNF, and cycled cathode; reproduced with permission.[155] Copyright 2018, Elsevier. (b) FTIR spectra of pristine and cycled PEGPE. Reproduced with permission.[156] Copyright 2018, Elsevier.

et al.[51] developed high-flux, flexible fibrous membranes by integrating electrospun nanofibers into a composite that combines the cathode, interlayer, and separator, effectively reducing interface issues while improving LiPSs confinement, electron transfer, and Li-ion diffusion (Fig. 12a). Post-mortem ICP-AES analysis (Fig. 12b) of anode after 400 cycles revealed significantly lower sulfur content, highlighting the composite membrane's superior polysulfide-trapping capability. The battery demonstrated an initial capacity of 1501 mA h g^{-1}, with a minimal capacity loss of 0.069% per cycle. To enhance safety in LiSBs Liu *et al.*[157] developed a thermally stable and non-flammable ZIF-L(Co) modified aramid nanofiber separator (Z-PMIA separator) using an electrospinning and *in situ* growth approach, which, as demonstrated by ICP-AES analysis after 350 cycles (Fig. 12c and d), significantly reduced Li$_2$S$_x$ deposition on the lithium anode compared to conventional PP separators. This superior performance resulted in an initial discharge capacity of 1391.2 mA h g^{-1}, with a minimal capacity fade of 0.033% per cycle.

3.4.4 Electron paramagnetic resonance (EPR). EPR, also known as Electron Spin Resonance (ESR), is a spectroscopic technique used to investigate materials with unpaired electrons (free radicals or transition metal ions) by exposing the sample to a magnetic field that causes these electrons to absorb electromagnetic radiation and transition between energy levels, resulting in the emission or absorption of microwaves.[160,161] In battery research, EPR is employed to analyze paramagnetic species like radicals and transition metal ions, providing essential insights into the composition, structure, and stability of the SEI layer, which are crucial for understanding and mitigating electrolyte decomposition and thus enhancing battery performance and longevity.[162] EPR identifies and quantifies redox-active species like lithium ions and radicals during cycling, offering insights into their concentration and behavior while also monitoring lithium dendrite formation on anodes to prevent short circuits and battery failure.[160]

Vacancy and interface engineering can significantly enhance the electronic structure and catalytic activity of metal chalcogenides, but their use in LiSBs is often limited by poor conductivity, loss of catalytic efficiency, and volumetric changes during cycling.[14] To address these issues, Ye *et al.* developed bimetallic chalcogenide nanosheet arrays (CoZn-X, where X = S, Se, Te) with abundant vacancies and heterointerfaces, (Fig. 13a–c) which aimed to improve ion transport and stabilize CoZn–S during electrocatalysis.[163] Post-mortem EPR spectra (Fig. 13d) revealed an increase in sulfur vacancies in CoZn–S after cycling, attributed to an induction period during initial sulfur conversion, enhancing catalytic activity. These nanosheet arrays exhibited a reversible capacity of 818 mA h
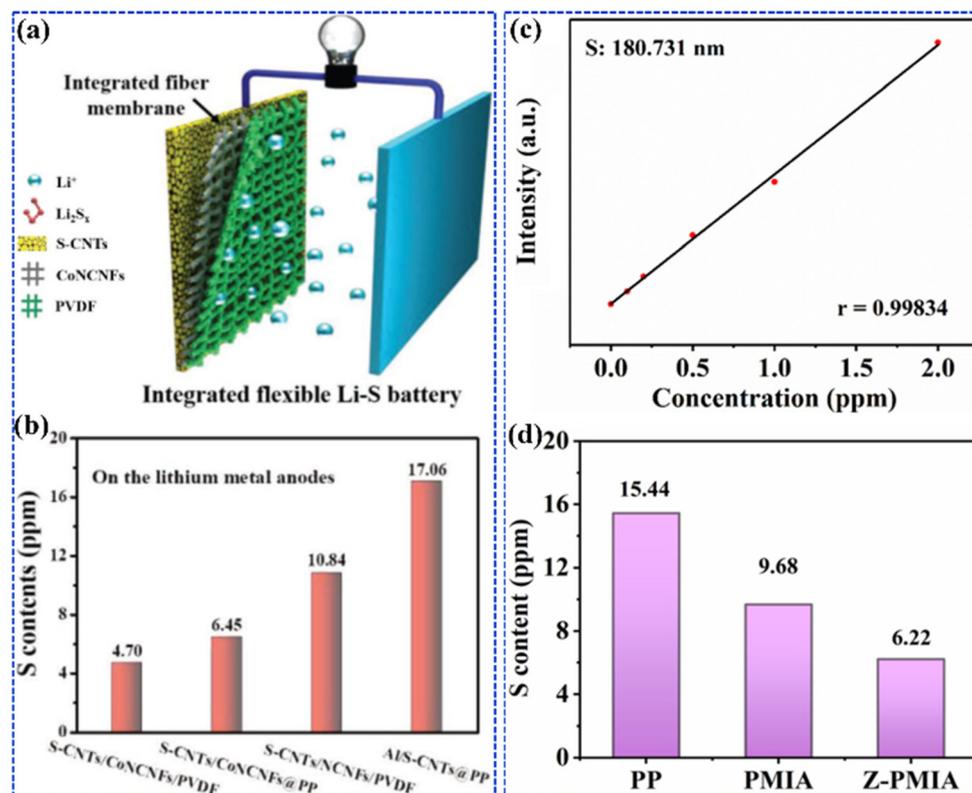
Fig. 12 (a) Schematic illustrations depicting the operational principles of flexible LiSBs, (b) S content in lithium metal anodes analyzed by ICP-AES after 400 cycles. Reproduced with permission.[51] Copyright 2019, Wiley-VCH. (c) S standard curve derived from ICP-AES; (d) S content of the cycled lithium metal anodes. Reproduced with permission.[157] Copyright 2021, Elsevier.
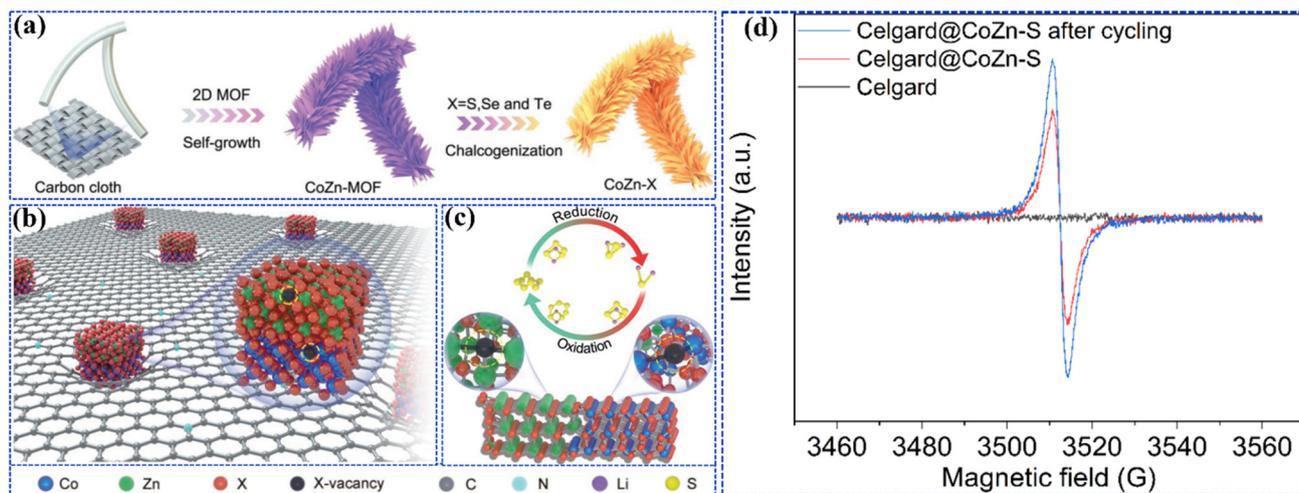
Fig. 13 Schematic of the: (a) preparation process for the CoZn-X and (b) structure evaluation demonstrating catalyst, anion vacancies and heterogeneous interfaces, (c) the mechanism for sulfur conversion and (d) EPR spectra of fresh CoZn-S and the cycled CoZn-S. Reproduced with permission.[163] Copyright 2022, Wiley-VCH.

g^{-1} over 110 cycles at 2 C with 90.9% retention, demonstrating that the engineered sulfur vacancies and interfacial fields in CoZn–S modulate the electronic structure and improve electron transfer rate.

3.4.5 Secondary-ion mass spectrometry (SIMS). SIMS characterizes the surface and near-surface composition of solid materials by using a focused primary ion beam to sputter atoms from the sample,[164] with the resulting secondary ions analyzed in a mass spectrometer to determine their mass-to-charge ratio (m/z), thereby providing detailed information about the elemental and molecular composition of the surface.[165] In battery research, SIMS is crucial for studying the distribution of lithium ions within electrode materials, offering insights into lithium diffusion behavior and distribution patterns of other elements, such as transition metals or impurities, which are essential for optimizing electrode design and understanding factors affecting battery performance and lifespan.[166,167]

To address challenges such as polysulfide shuttle, sluggish reaction kinetics, and dendritic lithium growth, He *et al.* devel-

oped a dual-function, flexible framework combining catalytic 1T′-MoTe$_2$ nanosheets with CNTs.[113] This framework supports both sulfur and metallic lithium and facilitates the formation of a thin, tellurized SEI primarily composed of lithium thiotellurate (Li_2TeS_3) when paired with a sulfur/MoTe$_2$-CNT cathode, thereby stabilizing lithium deposition and extending the battery cycle life. SIMS depth profiles after 50 cycles (Fig. 14) demonstrated that while the TeS– fragment from Li_2TeS_3 initially peaked sharply at 200 s and then decreased to 14% of its peak intensity by 8000 s, the LiTe– fragment from Li_2Te peaked rapidly at 420 s and remained stable with depth, and the Li– fragment showed a trend similar to the C– fragment, confirming uniform lithium plating and stripping.

3.4.6. Nuclear magnetic resonance (NMR) spectroscopy. NMR spectroscopy, a powerful technique for investigating molecular structure, dynamics, and interactions, exploits the nuclear spin of isotopes like hydrogen-1 and carbon-13, which absorb radiofrequency energy and transition between energy levels in a strong magnetic field, with the resulting signals revealing detailed information about the chemical environ-
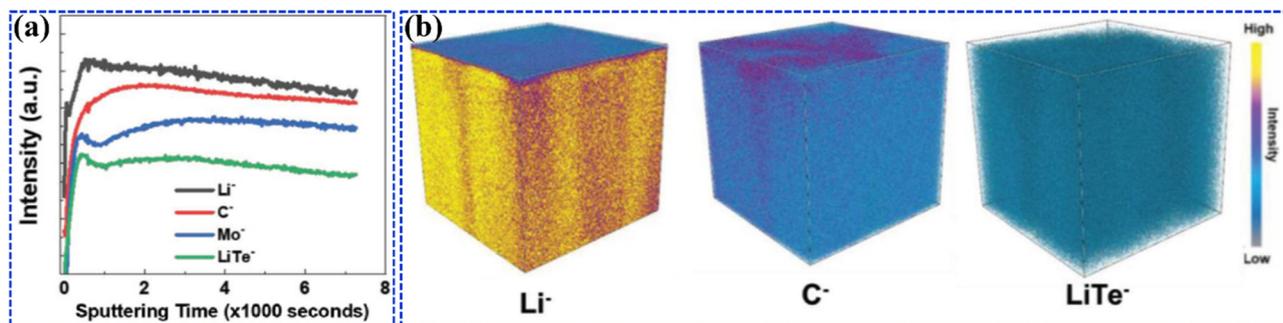
Fig. 14 After 50 cycles (a) depth profiles of various ions in MoTe$_2$-CNT/Li and (b) 3D imagining of the MoTe$_2$-CNT/Li. Reproduced with permission.[113] Copyright 2022, Wiley-VCH.

ment and molecular structure of the sample.[168,169] In battery research, this method is utilized to analyze the chemical composition and structural changes of electrode materials such as lithium cobalt oxide and graphite during cycling.[170] Grey *et al.*[171] used NMR spectroscopy to advance the understanding of LiSBs focusing on sulfur redox chemistry and structural changes during electrochemical cycling. This allows real-time monitoring of chemical reactions between elemental sulfur and polysulfides, the formation of the SEI, and lithium plating and stripping on the anode. By employing various NMR-active isotopes like ^{7}Li, ^{6}Li, and ^{3}S, researchers can detect the chemical environments of lithium species and track polysulfide formation throughout the charge–discharge process. The capability of ^{7}Li NMR to differentiate signals from lithium anodes and deposited metal enhances its utility for studying lithium dendrite formation, a significant issue impacting battery performance. Additionally, ^{3}S and ^{6}Li NMR techniques provide valuable insights into the formation of lithium sulfide and the behavior of polysulfides, respectively. By integrating these methodologies, the developed NMR setup offers qualitative and quantitative detection of lithium and sulfur species, elucidating the electrochemical processes within LiSBs. This comprehensive approach is vital for addressing capacity fade and enhancing the safety and efficiency of lithium–sulfur battery technologies. NMR also informs about the chemical environment of lithium ions in the electrolyte, aiding in optimizing electrolyte formulations for enhanced battery performance.[168] Additionally, NMR studies the behavior of other elements, like transition metals or impurities, in battery materials. For instance, Choudhury *et al.*[84] employed carbon onions to host a sulfur-rich copolymer synthesized *via* inverse vulcanization of sulfur and 1,3-diisopropenylbenzene (DIB). Post 100 galvanostatic cycles (Fig. 15), ^{1}H NMR spectroscopy revealed shifts in the 0.6–1.75 ppm range and new peaks at 2.17 and 2.29 ppm, indicating sulfide formation from copolymer fragmentation. Despite these changes, the copolymer maintained an initial capacity of 850 mA h g^{-1}, which

decreased to 585 mA h g^{-1} after 140 cycles, demonstrating its effectiveness as a sulfur source in LiSBs.

3.5 N$_2$ sorption isotherms

Nitrogen sorption isotherms are a fundamental technique for characterizing the pore structure and surface area of materials, achieved by exposing the sample to nitrogen gas under controlled pressures and temperatures, and subsequently measuring the quantity of gas adsorbed.[172–174] The resulting isotherm describes how nitrogen adsorption varies with pressure, providing information about pore size, shape, and distribution. In battery research, N$_2$ sorption isotherms characterize the porous structure of electrode materials, electrolytes, and separators.[175] These factors influence battery performance, particularly in electrolyte infiltration, ion transport, and electrode–electrolyte interface formation.[176]

For electrode materials, nitrogen sorption isotherms provide vital insights into the accessible surface area available for electrochemical reactions and electrolyte interaction, which are pivotal in understanding key performance metrics such as capacity, rate capability, and cycling stability.[177] When applied to electrolytes and separators, these isotherms are instrumental in characterizing porosity and permeability, parameters that are critical for effective electrolyte retention, ion transport, and the overall performance of the battery.[178] To elucidate the impact of binders on LiSB performance, Shafique *et al.* conducted a detailed study investigating the effects of different polymeric binders—polyethylene oxide (PEO), polyvinylidene difluoride (PVDF), and lithium polyacrylate (LiPAA)—each dispersed in specific solvents: PEO in acetonitrile (ACN), PVDF in *N*-methyl pyrrolidone (NMP), and LiPAA in an aqueous solution of water and alcohol.[179] The study focused on correlating binder types with the electrochemical behavior and morphological stability of sulfur electrodes, particularly under a sulfur
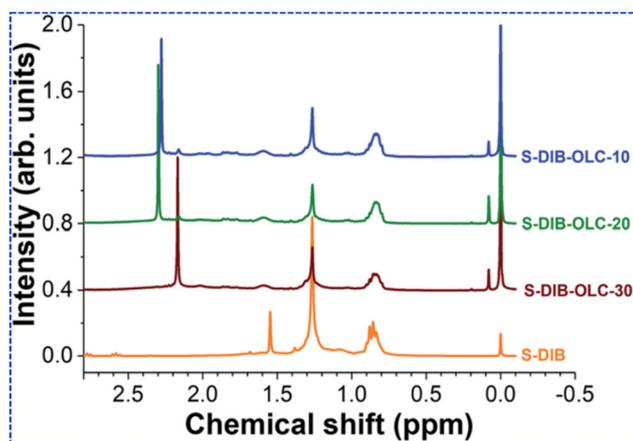
Fig. 15 ^{1}H NMR spectra after 100 cycles at 0.1 C. Reproduced with permission.[84] Copyright 2017, Royal Society of Chemistry.
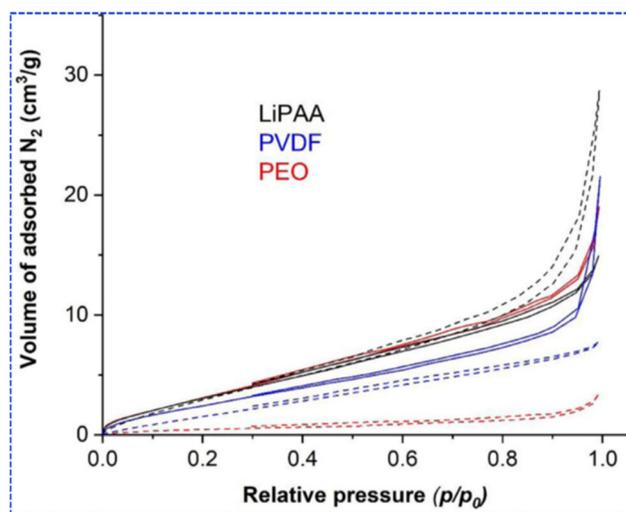
Fig. 16 Sorption isotherms of the pristine (solid lines) and cycled (2nd cycle, dashed lines) of different polymeric binder in LiSBs. Reproduced with permission.[179] Copyright 2020, Elsevier.

Table 4 Physio-chemical results obtained sorption isotherms. Reproduced with permission.[179] Copyright 2020, Elsevier

Sample	Surface area ($m^2 g^{-1}$)	Correlation coefficient	Pore volume ($cc g^{-1}$)	Pore size (nm)
Pristine LiPAA	22.9	0.99942	0.032	3
Pristine PVDF	15.3	0.99948	0.045	1.5
Pristine PEO	23.8	0.99999	0.037	3.6
Cycled LiPAA	23.4	0.99997	0.062	3.1
Cycled PVDF	14.6	0.99999	0.016	1.5
Cycled PEO	2.6	0.99991	0.007	4.3

loading of approximately 4.0 mg cm^{-2}, throughout the cycling process. N$_2$-sorption isotherms of pristine and cycled cells (Fig. 16) demonstrated that while fresh electrodes had similar surface areas, the sulfur electrodes with PEO binder experienced a significant decrease in surface area and pore volume by an order of magnitude after cycling, whereas electrodes with LiPAA and PVDF binders showed minimal changes, with less than 10% variation as indicated in Table 4. These BET results aligned with electrochemical data, which demonstrated that LiSBs with LiPAA experienced the least capacity fading and the highest reproducibility, ranking the binders as LiPAA > PVDF ≫ PEO, and in terms of electrochemical kinetics during cycling, LiPAA also outperformed PVDF and PEO, ranking LiPAA > PEO ≫ PVDF, confirming LiPAA as the superior binder for maintaining cell capacity stability and enhancing reaction kinetics.

4. Conclusions and perspectives

Post-mortem analysis of cycled LiSBs is indispensable for a comprehensive understanding of redox processes, the formation of new compounds and interfacial layers, and the identification of aging mechanisms—factors that are critical for optimizing existing materials and pioneering new functional materials. Before initiating cell disassembly or conducting post-mortem analysis, non-destructive electrochemical techniques provide critical insights into the evolving electrochemical behavior of cycled cells, thus laying a robust foundation for subsequent structural and chemical investigations. Techniques such as EIS offer valuable insights into cell impedance across various frequencies, highlighting changes in electrode reactions and electrolyte properties,[53] while CV provides information on redox reactions and reaction kinetics, helping to assess cell performance over cycles. The post-mortem analysis of LiSBs involves opening the cell and handling its air-sensitive components in an inert gas-filled glove box.[71] To start with, washing of the recovered electrodes in a solvent like DME, an electrolyte component, is recommended to preserve sample quality, though its impact on SEI layers is unclear. Initially recording optical images of cycled electrodes and separators helps track changes in color, shape, thickness, or size compared to fresh components. Cost-effective digital photography documents degradation, aiding researchers in identi-

fying trends and understanding mechanisms to develop mitigation strategies. Microscopic methods are essential for tracking changes in cycled cell components, offering high-resolution imaging that reveals structural and morphological alterations.[86] SEM examines surface morphology changes, such as cracks, voids, or particle size variations, to identify degradation mechanisms and failure modes.[63] TEM provides higher resolution images of electrode nanostructures and by-product formations like SEI layers or lithium dendrites, aiding in understanding their evolution and degradation trends.[77] AFM analyzes electrode surface morphology at the nanoscale, offering insights into surface roughness and film formation, which impact cell performance.[86] X-ray spectroscopy methods offer valuable insights into material chemical composition and electronic structure.[102] For example, XPS is commonly used to analyze electrode material surface chemistry before and after cycling, identifying elements and their chemical states by measuring emitted electron binding energies. This reveals changes in composition and oxidation states.[104,105] XRD provides information on phase changes, crystallographic defects, and new phase or compound formation in electrode material crystal structures during cycling. XANES gives insights into bonding and coordination environment changes of elements like sulfur, lithium, and transition metals.[131] XRF provides spatial distribution information of elements (sulfur, lithium, *etc.*) in electrodes critical for battery performance.[138] Optical spectroscopy methods offer detailed insights into the critical structural and chemical changes of electrode materials post-cycling. Raman spectra identify changes in chemical composition, phase transformation, and the formation of by-products like SEI layers or lithium dendrites.[25] FTIR spectra detail functional groups, chemical bonds, alterations in bonding, oxidation states, and new compound formation.[71] EDX offers distribution and concentration information of elements, revealing composition changes and by-product formation. ICP-AES determine elemental composition with high precision, crucial for studying active material and impurity concentration changes, providing insights into degradation mechanisms and material stability.[180] NMR reveals changes in bonding and molecular structure by examining the local environment of atoms in molecules.[170]

Looking forward, future research will likely prioritize improving the sensitivity, resolution, and efficiency of these analytical methods. As relatively new energy storage systems, lithium–sulfur batteries require further exploration of non-destructive techniques that are already well-established for LIBs. A few examples include:

4.1 Non-invasive current density imaging using magnetometry

Understanding current density is essential for analyzing SoC inhomogeneities, evaluating SEI thickness and formation, estimating heat generation, and addressing issues like uneven lithium-ion extraction and lithium plating. To advance this, Bason *et al.* introduced a non-invasive imaging technique to map intra-cell electrochemical activity using sensitive magnet-

ometers, allowing measurement of local current densities by analyzing external magnetic fields and offering insights into cell performance and safety.[181] Analyzing magnetic field maps of a lithium-ion battery under load (Fig. 17a) revealed current flow patterns influenced by overpotentials and impedance, enabling inference of critical cell properties such as lithiation state and diffusion coefficients from changes in magnetic field distribution.

4.2 Computational modeling

The integration of advanced analytical techniques with computational modeling holds great promise for the future of cycled cell analysis.[182] Computational models can simulate the complex electrochemical processes occurring within the cell, providing a theoretical framework for interpreting experimental data. By combining experimental results with computational simulations, researchers can gain deeper insights into the underlying mechanisms governing cell performance and degradation. This comprehensive strategy could result in the creation of predictive models to direct the design of advanced LiSBs with enhanced performance and durability.

4.3 Ultrasonic signals to predict state-of-charge

To elucidate the distribution of SoC in lithium-ion batteries, Huang *et al.*[183] employed an advanced acoustic method utilizing a focused ultrasound beam for cell scanning (Fig. 17b).
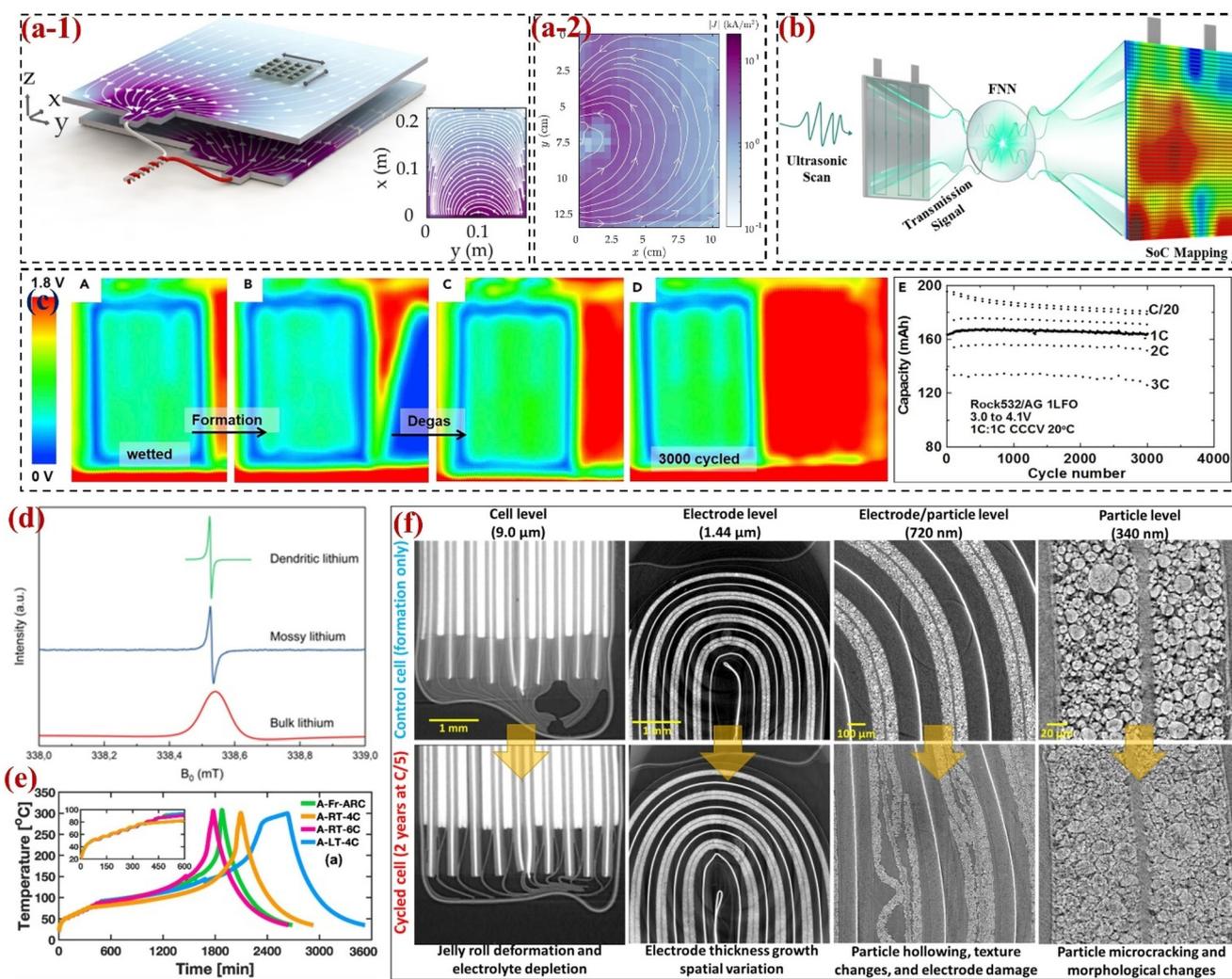
Fig. 17 (a-1) Current flow within LIB and corresponding magnetic field, (a-2) reconstructed current density image corresponding to a single electrode pair, during a 10A discharge with the battery tabs located at *x* = 0; Reproduced with permission.[181] Copyright 2022, Elsevier. (b) Schematic diagram of an ultrasonic scan of a LIB and analysis of SoC, reproduced with permission.[183] Copyright 2023, American Chemical Society. (c) Ultrasonic Images of a LIB with electrolyte: (A) after wetting, (B) post formation, (C) post degas, (D) after 3000 cycles, and (E) capacity *versus* cycle number. Reproduced with permission.[184] Copyright 2020, Elsevier. (d) First derivative CEPR signal, as measured in a field-swept EPR experiment, for metallic lithium with different morphologies. Reproduced with permission.[185] Copyright 2018, Springer Nature. (e) Time-dependent temperature profiles for pristine (green) and aged cells (orange, pink, and blue) at different C rates. Reproduced with permission.[187] Copyright 2025, Elsevier. (f) Full multi-scale comparison of polycrystalline NMC622/graphite pouch cell that was cycled for 2.5 years at C/5 from 3.0−4.1 V (bottom row) compared to control cell that was formation cycled only (top row). Reproduced with permission.[188] Copyright 2023, IOP publishing.

They analyzed the transmitted ultrasonic waves through a deep learning algorithm based on a feedforward neural network (FNN). This integration of progressive scanning with focused ultrasound enabled SoC mapping with an impressive in-plane resolution of 1 mm, a critical advancement for understanding battery failure mechanisms and facilitating the development of high-performance rechargeable batteries.

4.4 Ultrasonics to probe wetting of cells

Ultrasonic imaging technology, a non-destructive method for evaluating electrolytes and gases in pouch or prismatic cells, uses the fact that ultrasound attenuates more quickly in poorly wetted electrodes or separators to determine the minimum electrolyte injection volume and wetting time, optimizing the battery manufacturing process. It can also detect signs of electrolyte dry-out or unwetting in aged cells without disassembly, as gas can block ultrasound transmission. Deng and colleagues[184] employed a focused ultrasound beam with a diameter under 1 mm and achieved sub-millimeter resolution and 0.2 mm positional accuracy (Fig. 17c) to assess electrolyte wetting, dry-out, and unwetting.

4.5 Electron paramagnetic resonance (EPR) spectroscopy

EPR is a highly sensitive technique for detecting and characterizing lithium dendrites and plating, enabling the distinction between various lithium morphologies such as bulk, porous, and dendritic lithium. This is particularly useful for analyzing lithium metal in graphite anodes, where EPR can differentiate between active and "dead" lithium and provide quantitative insights into lithium deposition and lithiation processes.[185] Conduction EPR (CEPR) further enhances this capability by detecting conduction electrons, observing mossy lithium, and quantifying lithium plating. Niemoller et al. observed that the EPR spectrum of metallic lithium is influenced by the skin effect, which limits the penetration depth of microwave radiation.[185] This results in a Dysonian lineshape (Fig. 17d), with linewidth and intensity varying based on lithium morphology. Bulk lithium exhibits the broadest linewidth ($\sim$0.15 mT) with a Dysonian lineshape, while porous and dendritic lithium have progressively narrower linewidths, with mossy lithium at $\sim$0.03 mT and dendritic lithium showing the narrowest linewidth ($\sim$0.005 mT) and a Lorentzian lineshape due to its smaller particle size and surface characteristics.[186]

4.6 Accelerating rate calorimeter (ARC)

The ARC is a thermal analysis tool that evaluates the thermal behavior and safety of lithium-ion batteries under conditions leading to thermal runaway or failure.[189,190] By operating adiabatically, it minimizes heat loss, allowing accurate simulation of battery self-heating during exposure to rising temperatures and providing insights into exothermic reactions from short circuits, overcharging, or internal malfunctions.[191] This capability identifies critical temperature thresholds for thermal runaway—an uncontrolled energy release that can cause fires or explosions—and facilitates safe stress testing of batteries. The ARC also generates data on heat capacity and thermal reaction rates, essential for optimizing battery design, improving thermal management systems, and preventing hazards associated with thermal runaway, thereby enhancing overall battery reliability.[192] Manufacturers utilize ARC data to develop effective thermal management solutions and investigate failure modes linked to unwanted exothermic reactions. Huang et al.[193] conducted a detailed analysis of the thermal runaway behavior in LiSBs, from the pouch cell to the electrode level, using an ARC. Their study revealed that unlike in LIBs, thermal runaway in Li–S cells is initially triggered by reactions between sulfur cathode derivatives and the electrolyte solvent, particularly 1,3-dioxolane (DOL), rather than by the lithium anode. Interactions between the lithium metal anode, electrolyte, and molten sulfur species further accelerate these reactions. Notably, polysulfides were found to reduce the rapid self-heating rate at high temperatures during thermal runaway. Solvent vaporization was identified as the primary driver of internal pressure buildup before thermal runaway, while heat-induced gas release, including methane (CH_4) and ethylene (C_2H_4), intensified combustion in the later stages. The inherent thermal instability of the sulfur cathode and lithium anode, both prone to sublimation, melting, and cross-reactions at elevated temperatures, plays a critical role in determining the thermal runaway behavior. Even Li–S batteries with electrolytes of different thermal stabilities, including inorganic solid-state types, experienced rapid thermal runaway within a narrow temperature range due to inevitable melting-induced short circuits of the sulfur cathode and lithium anode. This in-depth understanding of thermal runaway mechanisms provides valuable insights for developing safer next-generation Li–S batteries. In a classic example in Fig. 17e, the time-dependent temperature profiles show that the A-Fr-ARC cell begins exothermic reactions at 92.04 °C and enters thermal runaway at 213.8 °C over 1317 minutes, ultimately reaching a maximum temperature of 308.0 °C.[187] In contrast, the aged A-RT-4C cell starts to exotherm at 77.06 °C, approximately 15 °C lower than the A-Fr-ARC, indicating the detrimental impact of lithium plating on thermal stability. This cell enters thermal runaway at 213.6 °C in 1682 minutes, exhibiting a similar T2 value to the A-Fr-ARC but with a longer time interval due to its lower T1 and an accelerated reaction rate from lithium deposition. Furthermore, the maximum temperature for the A-RT-4C cell is 300.7 °C, likely due to lithium plating depleting most electrolytes and reducing heat release during chemical reactions.

4.7 X-ray tomography

X-ray micro-computed tomography (micro-CT) is a high-resolution imaging technique that produces detailed three-dimensional representations of lithium-ion batteries at the microscale.[194,195] By using X-ray radiation to capture multiple two-dimensional projections from various angles, micro-CT reconstructs these images into a 3D volumetric view, enabling visualization of internal battery components like electrodes, electrolytes, and separators at micrometer resolution.[196] This technique leverages the differential attenuation of X-rays by different materials to identify variations in density and compo-

sition. In lithium-ion batteries, micro-CT is essential for studying structural evolution and degradation mechanisms during charge and discharge cycles, providing insights into phenomena such as lithium-ion transport, phase changes, and dendrite formation.[197] For instance, Fig. 17f illustrates CT scans of deep-cycled and control cells, revealing pervasive cathode microcracking.[188] This degradation process starts with microcracking, leading to particle swelling and a narrowing of the pore network, which increases tortuosity. The thickened cathode layer can push material beyond the aluminum current collector, expanding the jelly roll and damaging electrodes in confined spaces. Ultimately, this increases the pore volume of the cathode, which can result in electrolyte dry-out and roll-over failure if it exceeds the available electrolyte.

4.8 *Operando* analysis

In addition to ultrasonics and magnetometry, there is increasing interest in developing *operando* techniques that can monitor cycled cells under actual operating conditions.[43,198] For example, *in situ*/*operando* techniques including FTIR, Raman, XRD, XPS, ICP-AES, SIMS, and EIS enable researchers to observe dynamic changes in cell properties during cycling, offering a more comprehensive understanding of degradation mechanisms. Some of these *operando* analyses have not been reported for LiSBs which opens avenues for researchers to observe and understand the live transition within LiSBs while in operation.[28,199] Following are the various *operando* analytical techniques that have been used for batteries in general so far:

4.8.1. Operando X-ray diffraction (XRD). Operando X-ray diffraction (XRD) tracks structural changes in electrode materials by measuring diffraction patterns during lithiation and delithiation.[30] It is particularly effective for observing phase transitions in materials like nickel-rich NMC and LFP, revealing mechanical stress and potential capacity loss. This technique is critical for developing robust electrodes that enhance cycling stability and prevent degradation.[29]

4.8.2. *Operando* X-ray absorption spectroscopy (XAS). Operando X-ray absorption spectroscopy (XAS) examines oxidation states and local atomic environments of transition metals in electrodes during cycling.[200] It is valuable for studying materials like nickel and cobalt in cathodes, revealing redox reaction mechanisms and potential dissolution into the electrolyte. This insight helps optimize high-energy-density cathodes while minimizing degradation.

4.8.3. *Operando* neutron diffraction (ND). *Operando* neutron diffraction (ND) monitors lithium-ion movement by tracking their distribution in anodes and cathodes during cycling.[201] It is sensitive to light elements like lithium, revealing non-uniform lithiation and potential capacity fading.[202] This technique aids the development of high-capacity anodes, such as silicon, by identifying lithium transport pathways.

4.8.4. Operando transmission electron microscopy (TEM). *Operando* transmission electron microscopy (TEM) provides real-time imaging at the nanoscale, allowing direct observation of microstructural changes in electrodes.[203] It is particularly

useful for monitoring lithium dendrite formation and structural degradation in high-capacity materials like silicon anodes.[204] This visualization helps understand failure mechanisms and develop strategies for improved performance.[205]

4.8.5. *Operando* Raman spectroscopy. 4.7.5. *Operando* Raman spectroscopy detects vibrational modes in materials, providing insights into chemical changes during cycling.[206] It can monitor SEI formation on anodes and electrolyte decomposition, crucial for preventing side reactions.[207] By tracking SEI dynamics, this technique aids in optimizing electrolyte formulations and charging protocols to extend battery life.[208]

4.8.6. *Operando* nuclear magnetic resonance (NMR). *Operando* nuclear magnetic resonance (NMR) examines the local environment of lithium ions, revealing ion dynamics and concentration changes.[209] This technique tracks lithium-ion diffusion in electrodes and electrolytes, identifying bottlenecks such as sluggish transport. It is vital for solid-state batteries and high-capacity materials like silicon, to address lithium entrapment issues.

4.8.7. *Operando* synchrotron X-ray tomography offers. 4.7.7. *Operando* synchrotron X-ray tomography high-resolution 3D imaging of battery structures, visualizing defects and dendrite formation during cycling.[210,211] It can monitor crack and void development, aiding early detection of issues that lead to failure. This technique is essential for enhancing battery safety, especially in fast-charging applications.

4.8.8. *Operando* electrochemical impedance spectroscopy (EIS). *Operando* electrochemical impedance spectroscopy (EIS) measures battery impedance at various frequencies, providing insights into resistive and capacitive behavior.[31,37,212] It tracks internal resistance changes of the SEI layer and lithium-ion diffusion kinetics, crucial for optimizing cycling conditions and minimizing impedance growth, which can lead to power loss.

4.8.9. *Operando* Fourier transform infrared (FTIR) spectroscopy. *Operando* Fourier transform infrared (FTIR) spectroscopy measures the absorption of infrared radiation, offering insights into molecular structure changes.[213] It monitors electrolyte decomposition and SEI formation on anodes, tracking reactions that influence battery performance.[214] This technique aids in optimizing electrolyte formulations to improve battery stability and lifespan.

4.8.10. *Operando* cyclic voltammetry (CV). *Operando* cyclic voltammetry (CV) measures the current response to varying voltage, providing insights into redox reactions and charge-transfer kinetics.[38] It is useful for studying electrode behavior and identifying potential side reactions during cycling. CV helps optimize electrode materials by assessing electrochemical performance and efficiency.

4.8.11. *Operando* UV-visible spectroscopy. *Operando* UV-visible spectroscopy measures light absorption, offering insights into the electronic structure of materials.[215] It tracks redox reactions in transition metals during cycling, revealing oxidation state changes critical for material performance. This technique aids in optimizing high-capacity cathodes and identifying factors contributing to capacity fading.[35]

Table 5 Summary of analytical techniques and the phenomena they can identify

Method	Sensitivity	Depth profiling	Detection of Li	Growth of films on electrodes	Clogging of pores	Delamination of electrode or separator	Cracks in electrode coating	Deformation of electrodes	Change/films on particle surfaces	Particle cracks	Exfoliation	Dissolution/migration of transition metals	Electrolyte degradation
				Electrode/separator degradation					Material degradation				
SEM	Surface	No	No	Yes	No	Yes	Yes	Yes	Yes	Yes	Yes	No	No
TEM	Surface	No	No	Yes	No	No	No	No	Yes	Yes	Yes	No	No
AFM	Surface	Yes	No	Yes	No	No	No	No	No	No	No	No	No
Optical imaging	Surface	No	No	Yes	Limited	Yes	Yes	Yes	No	No	No	No	No
XPS	Surface	Limited	Yes	Yes	No	No	No	No	No	No	No	No	No
XRD	Bulk	No	No	Limited	No	No	No	No	Limited	Limited	No	No	No
XANES	Bulk	No	No	No	No	No	No	No	Yes	No	No	No	No
XRF	Surface/bulk	Limited	No	Yes	No	No	No	No	Yes	No	No	Yes	No
RAMAN	Surface/bulk	Limited	No	Yes	No	No	No	No	Yes	No	No	No	No
FTIR	Surface/bulk	No	No	Yes	No	No	No	No	No	No	No	No	Limited
EDX	Surface	No	No	Yes	No	No	No	No	Yes	No	No	Yes	No
ICP-AES	Bulk	No	Yes	Limited	No	No	No	No	Yes	No	No	Yes	No
EPR	Surface	Limited	Yes	No	No	No	No	No	Yes	No	No	No	No
SIMS	Surface/bulk	No	Yes	Yes	No	No	No	No	Yes	No	No	Yes	No
NMR	Bulk	No	Yes	No	No	No	No	No	Limited	No	No	No	Yes
BET	Bulk	No	No	No	Yes	No	No	No	No	No	No	No	No

Legend: YES | NO | LIMITED

4.8.12. *Operando* X-ray photoelectron spectroscopy (XPS). *Operando* X-ray photoelectron spectroscopy (XPS) analyzes core electron binding energies, providing information about elemental composition and chemical states.[32,33] It tracks changes at the electrode–electrolyte interface, especially in SEI layer evolution.[34] This technique is crucial for optimizing electrode materials and enhancing battery performance and stability.[211]

4.8.13. *Operando* infrared (IR) thermography. *Operando* infrared (IR) thermography detects temperature changes on battery surfaces during operation.[216] It is valuable for monitoring overheating and identifying hot spots that could lead to thermal runaway. By mapping temperature distributions, this technique aids in designing thermal management systems for safer lithium-ion batteries.

4.8.14. *Operando* inductively coupled plasma optical emission spectroscopy (ICP-OES). *Operando* inductively coupled plasma optical emission spectroscopy (ICP-OES) quantifies elemental compositions in samples by analyzing emitted light from excited elements.[38] It monitors metal dissolution from cathodes during operation, addressing issues that contribute to capacity fading. This technique is essential for studying cathode stability and optimizing electrolyte formulations.

4.8.15. *Operando* electron paramagnetic resonance (EPR). Operando electron paramagnetic resonance (EPR) detects unpaired electrons, providing insights into oxidation states and electronic structures. It monitors lithium dendrite formation and identifies crystal structure defects in electrode materials.[217] EPR is useful for improving fast-charging protocols by preventing dendrite growth and enhancing battery safety.[218]

4.8.16. *Operando* mass spectrometry (MS). *Operando* mass spectrometry (MS) analyzes mass-to-charge ratios, detecting gas evolution and electrolyte decomposition products.[33,219] This technique monitors gas generation during cycling, identifying conditions leading to undesirable side reactions. MS aids in designing safer batteries by improving electrolyte stability under high voltage and temperature conditions.

As observed in the pie-chart in Scheme 1, although more research involving post-mortem analysis is being conceded, a huge number of important analytical techniques remain under-represented which need to be equally explored. In addition, we have observed in Table 5 that a single technique is not enough to gather all the important information required from the cycled cell. Thus, it becomes highly desirable to use a combination of these post-mortem techniques to analyze the cell from every perspective ranging from the structural, chemical, and electronic changes occurring within the cells. In addition, analyzing the cycled cells during post-mortem analysis offers invaluable benefits in understanding the degradation mechanisms and failure modes of battery materials. This understanding is vital for devising methods to boost battery efficiency, reliability, and longevity. Additionally, post-mortem analysis provides a thorough insight into the factors driving cell deterioration, promoting the advancement of more effective and resilient battery technologies for diverse applications.

Data availability

No primary research results, software or code have been included and no new data were generated or analysed as part of this review.

Conflicts of interest

There are no conflicts to declare.

Acknowledgements

References

1 S. Kim, G. Park, S. J. Lee, S. Seo, K. Ryu, C. H. Kim and J. W. Choi, *Adv. Mater.*, 2023, **35**, 2206625.

2 J. Kim, Y. Kim, J. Yoo, G. Kwon, Y. Ko and K. Kang, *Nat. Rev. Mater.*, 2022, **8**, 54–70.

3 Z. P. Cano, D. Banham, S. Ye, A. Hintennach, J. Lu, M. Fowler and Z. Chen, *Nat. Energy*, 2018, **3**, 279–289.

4 R. Schmuch, R. Wagner, G. Hörpel, T. Placke and M. Winter, *Nat. Energy*, 2018, **3**, 267–278.

5 J. W. Choi and D. Aurbach, *Nat. Rev. Mater.*, 2016, **1**, 1–16.

6 G. Zhou, H. Chen and Y. Cui, *Nat. Energy*, 2022, **7**, 312–319.

7 H. Li, R. Meng, C. Ye, A. Tadich, W. Hua, Q. Gu, B. Johannessen, X. Chen, K. Davey and S. Z. Qiao, *Nat. Nanotechnol.*, 2024, **2024**, 1–8.

8 Y. Chen, T. Wang, H. Tian, D. Su, Q. Zhang and G. Wang, *Adv. Mater.*, 2021, **33**, 2003666.

9 Q. Pang, X. Liang, C. Y. Kwok and L. F. Nazar, *Nat. Energy*, 2016, **1**, 1–11.

10 M. Jana, R. Xu, X. B. Cheng, J. S. Yeon, J. M. Park, J. Q. Huang, Q. Zhang and H. S. Park, *Energy Environ. Sci.*, 2020, **13**, 1049–1075.

11 B. Liu, H. Gu, J. F. Torres, Z. Yin and A. Tricoli, *Energy Environ. Sci.*, 2024, **17**, 1073–1082.

12 Y. X. Song, Y. Shi, J. Wan, S. Y. Lang, X. C. Hu, H. J. Yan, B. Liu, Y. G. Guo, R. Wen and L. J. Wan, *Energy Environ. Sci.*, 2019, **12**, 2496–2506.

13 Z. L. Xu, S. J. Kim, D. Chang, K. Y. Park, K. S. Dae, K. P. Dao, J. M. Yuk and K. Kang, *Energy Environ. Sci.*, 2019, **12**, 3144–3155.

14 Y. Guo, Q. Niu, F. Pei, Q. Wang, Y. Zhang, L. Du, Y. Zhang, Y. Zhang, Y. Zhang, L. Fan, Q. Zhang, L. Yuan and Y. Huang, *Energy Environ. Sci.*, 2024, **17**, 1330–1367.

15 M. Wild, L. O'Neill, T. Zhang, R. Purkayastha, G. Minton, M. Marinescu and G. J. Offer, *Energy Environ. Sci.*, 2015, **8**, 3477–3494.

16 G. Zhou, F. Li and H. M. Cheng, *Energy Environ. Sci.*, 2014, **7**, 1307–1338.

17 J. Guo, Q. Yang, Y. Dou, X. Ba, W. Wei and J. Liu, *Energy Environ. Sci.*, 2024, **17**(5), 1695–1724.

18 V. K. Tomer, O. A. T. Dias, A. M. Gouda, R. Malik and M. Sain, *Mater. Horiz.*, 2024, **11**, 3090–3103.

19 L. A. Middlemiss, A. J. R. Rennie, R. Sayers and A. R. West, *Energy Rep.*, 2020, **6**, 232–241.

20 X. Yang and A. L. Rogach, *Adv. Energy Mater.*, 2019, **9**, 1900747.

21 X. Li, S. Liu, J. Yang, Z. He, J. Zheng and Y. Li, *Energy Storage Mater.*, 2023, **55**, 606–630.

22 H. A. Petersen, T. H. T. Myren, S. J. O'Sullivan and O. R. Luca, *Mater. Adv.*, 2021, **2**, 1113–1138.

23 N. Meddings, M. Heinrich, F. Overney, J. S. Lee, V. Ruiz, E. Napolitano, S. Seitz, G. Hinds, R. Raccichini, M. Gaberšček and J. Park, *J. Power Sources*, 2020, **480**, 228742.

24 Y. H. Lin, S. J. Ruan, Y. X. Chen and Y. F. Li, *Renewable Sustainable Energy Rev.*, 2023, **188**, 113807.

25 S. Lang, S. H. Yu, X. Feng, M. R. Krumov and H. D. Abruña, *Nat. Commun.*, 2022, **13**, 1–11.

26 S. Zhou, J. Shi, S. Liu, G. Li, F. Pei, Y. Chen, J. Deng, Q. Zheng, J. Li, C. Zhao, I. Hwang, C. J. Sun, Y. Liu, Y. Deng, L. Huang, Y. Qiao, G. L. Xu, J. F. Chen, K. Amine, S. G. Sun and H. G. Liao, *Nature*, 2023, **621**, 75–81.

27 S. H. Yu, X. Huang, K. Schwarz, R. Huang, T. A. Arias, J. D. Brock and H. D. Abruña, *Energy Environ. Sci.*, 2018, **11**, 202–210.

28 F. Schomburg, B. Heidrich, S. Wennemar, R. Drees, T. Roth, M. Kurrat, H. Heimes, A. Jossen, M. Winter, J. Y. Cheong and F. Röder, *Energy Environ. Sci.*, 2024, **17**, 2686–2733.

29 Y. Liu, H. Shi and Z. S. Wu, *Energy Environ. Sci.*, 2023, **16**, 4834–4871.

30 A. Grant and C. O'dwyer, *Appl. Phys. Rev.*, 2023, **10**, 11312.

31 A. M. Tripathi, W. N. Su and B. J. Hwang, *Chem. Soc. Rev.*, 2018, **47**, 736–851.

32 J. Tan, D. Liu, X. Xu and L. Mai, *Nanoscale*, 2017, **9**, 19001–19016.

33 Y. Yang, J. Feijóo, V. Briega-Martos, Q. Li, M. Krumov, S. Merkens, G. De Salvo, A. Chuvilin, J. Jin, H. Huang, C. J. Pollock, M. B. Salmeron, C. Wang, D. A. Muller, H. D. Abruña and P. Yang, *Curr. Opin. Electrochem.*, 2023, **42**, 101403.

34 J. Maibach, J. Rizell, A. Matic and N. Mozhzhukhina, *ACS Mater. Lett.*, 2023, **5**, 2431–2444.

35 H. Li, S. Guo and H. Zhou, *J. Energy Chem.*, 2021, **59**, 191–211.

36 S. Rehman, M. Pope, S. Tao and E. McCalla, *Energy Environ. Sci.*, 2022, **15**, 1423–1460.

37 J. H. Tian, T. Jiang, M. Wang, Z. Hu, X. Zhu, L. Zhang, T. Qian and C. Yan, *Small Methods*, 2020, **4**, 1900467.

38 T. J. Leckie, S. D. Robertson and E. Brightman, *Energy Adv.*, 2024, **3**(10), 2479–2502.

39 M. Yousaf, U. Naseer, Y. Li, Z. Ali, N. Mahmood, L. Wang, P. Gao and S. Guo, *Energy Environ. Sci.*, 2021, **14**, 2670–2707.

40 S. Rehman, M. Pope, S. Tao and E. McCalla, *Energy Environ. Sci.*, 2022, **15**, 1423–1460.

41 Y. Ma, S. Li and B. Wei, *Nanoscale*, 2019, **11**, 20429–20436.

42 S. K. Park, W. M. Dose, D. Boruah, M. De Volder, S. K. Park, W. M. Dose, B. D. Boruah and M. De Volder, *Adv. Mater. Technol.*, 2022, **7**, 2100799.

43 F. Strauss, D. Kitsche, Y. Ma, J. H. Teo, D. Goonetilleke, J. Janek, M. Bianchini and T. Brezesinski, *Adv. Energy Sustainability Res.*, 2021, **2**, 2100004.

44 C. Pastor-Fernández, T. F. Yu, W. D. Widanage and J. Marco, *Renewable Sustainable Energy Rev.*, 2019, **109**, 138–159.

45 A. Grant and C. O'dwyer, *Appl. Phys. Rev.*, 2023, **10**, 11312.

46 Y. Li, J. Guo, K. Pedersen, L. Gurevich and D. I. Stroe, *Batteries*, 2022, **8**, 72.

47 H. Park, O. Tamwattana, J. Kim, S. Buakeaw, R. Hongtong, B. Kim, P. Khomein, G. Liu, N. Meethong and K. Kang, *Adv. Energy Mater.*, 2021, **11**, 2003039.

48 X. Lin, K. Khosravinia, X. Hu, J. Li and W. Lu, *Prog. Energy Combust. Sci.*, 2021, **87**, 100953.

49 T. Waldmann, A. Iturrondobeitia, M. Kasper, N. Ghanbari, F. Aguesse, E. Bekaert, L. Daniel, S. Genies, I. J. Gordon, M. W. Löble, E. De Vito and M. Wohlfahrt-Mehrens, *J. Electrochem. Soc.*, 2016, **163**, A2149–A2164.

50 F. Wu, F. Chu, G. A. Ferrero, M. Sevilla, A. B. Fuertes, O. Borodin, Y. Yu and G. Yushin, *Nano Lett.*, 2020, **20**, 5391–5399.

51 J. Wang, G. Yang, J. Chen, Y. Liu, Y. Wang, C. Y. Lao, K. Xi, D. Yang, C. J. Harris, W. Yan, S. Ding and R. V. Kumar, *Adv. Energy Mater.*, 2019, **9**, 1902001.

52 C. Wei, M. Tian, Z. Fan, L. Yu, Y. Song, X. Yang, Z. Shi, M. Wang, R. Yang and J. Sun, *Energy Storage Mater.*, 2021, **41**, 141–151.

53 P. Vadhva, J. Hu, M. J. Johnson, R. Stocker, M. Braglia, D. J. L. Brett and A. J. E. Rettie, *ChemElectroChem*, 2021, **8**, 1930–1947.

54 L. Stolz, M. Gaberšček, M. Winter and J. Kasnatscheew, *Chem. Mater.*, 2022, **34**, 10272–10278.

55 W. Choi, H. C. Shin, J. M. Kim, J. Y. Choi and W. S. Yoon, *J. Electrochem. Sci. Technol.*, 2020, **11**, 1–13.

56 O. A. T. Dias, F. Azarnia, K. Rathi, V. Pakharenko, V. K. Tomer and M. Sain, *Nanoscale*, 2024, **16**(34), 16003–16014.

57 X. Huang, B. Luo, R. Knibbe, H. Hu, M. Lyu, M. Xiao, D. Sun, S. Wang and L. Wang, *Chem. – Eur. J.*, 2018, **24**, 18544–18550.

58 Y. Huang, M. Shaibani, T. D. Gamot, M. Wang, P. Jovanović, M. C. Dilusha Cooray, M. S. Mirshekarloo, R. J. Mulder, N. V. Medhekar, M. R. Hill and M. Majumder, *Nat. Commun.*, 2021, **12**, 1–15.

59 N. Elgrishi, K. J. Rountree, B. D. McCarthy, E. S. Rountree, T. T. Eisenhart and J. L. Dempsey, *J. Chem. Educ.*, 2018, **95**, 197–206.

60 X. Huang, Z. Wang, R. Knibbe, B. Luo, S. A. Ahad, D. Sun and L. Wang, *Energy Technol.*, 2019, **7**, 1801001.

61 X. Huang, Z. Wang, R. Knibbe, B. Luo, S. A. Ahad, D. Sun and L. Wang, *Energy Technol.*, 2019, **7**, 1801001.

62 J. Wu, M. Fenech, R. F. Webster, R. D. Tilley and N. Sharma, *Sustainable Energy Fuels*, 2019, **3**, 1623–1646.

63 E. Ventosa and W. Schuhmann, *Phys. Chem. Chem. Phys.*, 2015, **17**, 28441–28450.

64 M. Zhang, M. Chouchane, S. A. Shojaee, B. Winiarski, Z. Liu, L. Li, R. Pelapur, A. Shodiev, W. Yao, J. M. Doux, S. Wang, Y. Li, C. Liu, H. Lemmens, A. A. Franco and Y. S. Meng, *Joule*, 2023, **7**, 201–220.

65 Z. Deng, X. Lin, Z. Huang, J. Meng, Y. Zhong, G. Ma, Y. Zhou, Y. Shen, H. Ding and Y. Huang, *Adv. Energy Mater.*, 2021, **11**, 2000806.

66 M. Biton, V. Yufit, F. Tariq, M. Kishimoto and N. Brandon, *J. Electrochem. Soc.*, 2017, **164**, A6032–A6038.

67 X. Liu, L. Zhang, H. Yu, J. Wang, J. Li, K. Yang, Y. Zhao, H. Wang, B. Wu, N. P. Brandon and S. Yang, *Adv. Energy Mater.*, 2022, **12**, 2200889.

68 C. Tian, B. Li, X. Hu, J. Wu, P. Li, X. Xiang, X. Zu and S. Li, *ACS Appl. Mater. Interfaces*, 2021, **13**, 6229–6240.

69 Y. Song, X. Long, Z. Luo, C. Guo, C. N. Geng, Q. S. Ouyang, Z. Han, G. Zhou and J. J. Shao, *ACS Appl. Mater. Interfaces*, 2022, **14**, 32183–32195.

70 X. Chen, Y. Wang, J. Wang, J. Liu, S. Sun, L. Zhu, Q. Ma, N. Zhu, X. Wang, J. Chen and W. Yan, *J. Mater. Chem. A*, 2022, **10**, 1359–1368.

71 É. A. Santos, C. G. Anchieta, R. C. Fernandes, M. J. Pinzón, A. N. Miranda, I. Galantini, F. C. B. Maia, G. Doubek, C. B. Rodella, L. M. Da Silva and H. Zanin, *Nano Energy*, 2023, **116**, 108809.

72 Y. Liu, H. Liu, Y. Lin, Y. Zhao, H. Yuan, Y. Su, J. Zhang, S. Ren, H. Fan and Y. Zhang, *Adv. Funct. Mater.*, 2021, **31**, 2104863.

73 C. Geng, W. Qu, Z. Han, L. Wang, W. Lv and Q. H. Yang, *Adv. Energy Mater.*, 2023, **13**, 2204246.

74 P. Xiong, S. Zhang, R. Wang, L. Zhang, Q. Ma, X. Ren, Y. Gao, Z. Wang, Z. Guo and C. Zhang, *Energy Environ. Sci.*, 2023, **16**, 3181–3213.

75 Z. J. Zheng, H. Ye and Z. P. Guo, *Energy Environ. Sci.*, 2021, **14**, 1835–1853.

76 L. Tian, Z. Zhang, S. Liu, G. Li and X. Gao, *Energy Environ. Mater.*, 2022, **5**, 645–654.

77 Y. Cheng, L. Zhang, Q. Zhang, J. Li, Y. Tang, C. Delmas, T. Zhu, M. Winter, M. S. Wang and J. Huang, *Mater. Today*, 2021, **42**, 137–161.

78 T. Shang, Y. Wen, D. Xiao, L. Gu, Y. S. Hu and H. Li, *Adv. Energy Mater.*, 2017, **7**, 1700709.

79 Z. Fan, L. Zhang, D. Baumann, L. Mei, Y. Yao, X. Duan, Y. Shi, J. Huang, Y. Huang and X. Duan, *Adv. Mater.*, 2019, **31**, 1900608.

80 X. Wu, S. Li, B. Yang and C. Wang, *Electrochem. Energy Rev.*, 2019, **2**, 467–491.

81 M. Yousaf, U. Naseer, Y. Li, Z. Ali, N. Mahmood, L. Wang, P. Gao and S. Guo, *Energy Environ. Sci.*, 2021, **14**, 2670–2707.

82 R. Pai, A. Singh, M. H. Tang and V. Kalra, *Commun. Chem.*, 2022, **5**, 1–11.

83 J. Y. Hwang, H. M. Kim, S. Shin and Y. K. Sun, *Adv. Funct. Mater.*, 2018, **28**, 1704294.

84 S. Choudhury, P. Srimuk, K. Raju, A. Tolosa, S. Fleischmann, M. Zeiger, K. I. Ozoemena, L. Borchardt and V. Presser, *Sustainable Energy Fuels*, 2017, **2**, 133–146.

85 S. Wang, Q. Liu, C. Zhao, F. Lv, X. Qin, H. Du, F. Kang and B. Li, *Energy Environ. Mater.*, 2018, **1**, 28–40.

86 Z. Zhang, S. Said, K. Smith, R. Jervis, C. A. Howard, P. R. Shearing, D. J. L. Brett, T. S. Miller, Z. Zhang, S. Said,

K. Smith, R. Jervis, P. R. Shearing, D. J. L. Brett and T. S. Miller, *Adv. Energy Mater.*, 2021, **11**, 2101518.

87 M. Wang, Z. Song, J. Bi, H. Li, M. Xu, Y. Gong, Y. Zhou, Y. Zhao and K. Yang, *Battery Energy*, 2023, **2**, 20230006.

88 W. Chen, X. Chen, W. Chen and Z. Jiang, *Energy Technol.*, 2023, **11**, 2201372.

89 Z. Deng, X. Lin, Z. Huang, J. Meng, Y. Zhong, G. Ma, Y. Zhou, Y. Shen, H. Ding and Y. Huang, *Adv. Energy Mater.*, 2021, **11**, 2000806.

90 W. Liu, P. Liu and D. Mitlin, *Adv. Energy Mater.*, 2020, **10**, 2002297.

91 W. Liu, P. Liu and D. Mitlin, *Chem. Soc. Rev.*, 2020, **49**, 7284–7300.

92 C. Senthil, S. G. Kim, S. S. Kim, M. G. Hahm and H. Y. Jung, *Small*, 2022, **18**, 2200919.

93 J. Wang, S. Yi, J. Liu, S. Sun, Y. Liu, D. Yang, K. Xi, G. Gao, A. Abdelkader, W. Yan, S. Ding and R. V. Kumar, *ACS Nano*, 2020, **14**, 9819–9831.

94 F. Wu, J. Maier and Y. Yu, *Chem. Soc. Rev.*, 2020, **49**, 1569–1614.

95 Z. Chang, Y. Qiao, H. Deng, H. Yang, P. He and H. Zhou, *Energy Environ. Sci.*, 2020, **13**, 1197–1204.

96 D. Lin, Y. Liu and Y. Cui, *Nat. Nanotechnol.*, 2017, **12**, 194–206.

97 Q. Zeng, X. Li, W. Gong, S. Guo, Y. Ouyang, D. Li, Y. Xiao, C. Tan, L. Xie, H. Lu, Q. Zhang and S. Huang, *Adv. Energy Mater.*, 2022, **12**, 2104074.

98 H. Cheng, Z. Shen, W. Liu, M. Luo, F. Huo, J. Hui, Q. Zhu and H. Zhang, *ACS Nano*, 2023, **17**, 14695–14705.

99 G. Jiménez-Martín, J. Castillo, X. Judez, J. L. Gómez-Urbano, G. Moreno-Fernández, A. Santiago, A. Saenz de Buruaga, I. Garbayo, J. A. Coca-Clemente, A. Villaverde, M. Armand, C. Li and D. Carriazo, *Batteries Supercaps*, 2022, **5**, e202200167.

100 M. Xu, T. Wu, J. Qi, D. Zhou and Z. Xiao, *J. Mater. Chem. A*, 2021, **9**, 21429–21439.

101 M. Fehse, A. Iadecola, L. Simonelli, A. Longo and L. Stievano, *Phys. Chem. Chem. Phys.*, 2021, **23**, 23445–23465.

102 B. F. Baggio and Y. Grunder, *Annu. Rev. Anal. Chem.*, 2021, **14**, 87–107, DOI: **10.1146/annurev-anchem-091020-100631**.

103 V. K. Tomer, R. L. Kumawat, O. A. Titton Dias, R. Malik, G. C. Schatz and M. Sain, *J. Mater. Chem. A*, 2024, **12**, 15814–15828.

104 V. Shutthanandan, M. Nandasiri, J. Zheng, M. H. Engelhard, W. Xu, S. Thevuthasan and V. Murugesan, *J. Electron Spectrosc. Relat. Phenom.*, 2019, **231**, 2–10.

105 V. Shutthanandan, M. Nandasiri, J. Zheng, M. H. Engelhard, W. Xu, S. Thevuthasan and V. Murugesan, *J. Electron Spectrosc. Relat. Phenom.*, 2019, **231**, 2–10.

106 F. Yang, X. Feng, Y. S. Liu, L. C. Kao, P. A. Glans, W. Yang and J. Guo, *Energy Environ. Mater.*, 2021, **4**, 139–157.

107 I. Källquist, R. Le Ruyet, H. Liu, R. Mogensen, M. T. Lee, K. Edström and A. J. Naylor, *J. Mater. Chem. A*, 2022, **10**, 19466–19505.

108 S. Louisia, M. T. M. Koper and R. V. Mom, *Curr. Opin. Electrochem.*, 2024, 101462.

109 G. Greczynski, R. T. Haasch, N. Hellgren, E. Lewin and L. Hultman, *Nat. Rev. Methods Primers*, 2023, **3**, 1–19.

110 H. Du, S. Li, H. Qu, B. Lu, X. Wang, J. Chai, H. Zhang, J. Ma, Z. Zhang and G. Cui, *J. Membr. Sci.*, 2018, **550**, 399–406.

111 J. Wang, Q. Ma, S. Sun, K. Yang, Q. Cai, E. Olsson, X. Chen, Z. Wang, A. M. Abdelkader, Y. Li, W. Yan, S. Ding and K. Xi, *eScience*, 2022, **2**, 655–665.

112 D. Dutta Pathak, B. P. Mandal and A. K. Tyagi, *J. Power Sources*, 2021, **488**, 229456.

113 J. He, A. Bhargav and A. Manthiram, *Adv. Energy Mater.*, 2022, **12**, 2103204.

114 Y. Zhou, C. H. Wang, W. Lu and L. Dai, *Adv. Mater.*, 2020, **32**, 1902779.

115 X. Zhou, B. Liu, Y. Chen, L. Guo and G. Wei, *Mater. Adv.*, 2020, **1**, 2163–2181.

116 Y. C. Chien, A. S. Menon, W. R. Brant, M. J. Lacey and D. Brandell, *J. Phys. Chem. C*, 2022, **126**, 2971–2979.

117 G. Tonin, G. B. M. Vaughan, R. Bouchet, F. Alloin, M. Di Michiel and C. Barchasz, *J. Power Sources*, 2020, **468**, 228287.

118 S. Lang, X. Feng, J. Seok, Y. Yang, M. R. Krumov, A. Molina Villarino, M. A. Lowe, S. H. Yu and H. D. Abruña, *Curr. Opin. Electrochem.*, 2021, **25**, 100652.

119 M. Xia, T. Liu, N. Peng, R. Zheng, X. Cheng, H. Zhu, H. Yu, M. Shui and J. Shu, *Small Methods*, 2019, **3**, 1900119.

120 J. S. Yeon, S. Yun, J. M. Park and H. S. Park, *ACS Nano*, 2019, **13**, 5163–5171.

121 W. Yao, J. Xu, Y. Cao, Y. Meng, Z. Wu, L. Zhan, Y. Wang, Y. Zhang, I. Manke, N. Chen, C. Yang and R. Chen, *ACS Nano*, 2022, **16**, 10783–10797.

122 W. Yao, W. Zheng, J. Xu, C. Tian, K. Han, W. Sun and S. Xiao, *ACS Nano*, 2021, **15**, 7114–7130.

123 S. Archana and P. Elumalai, *Langmuir*, 2023, **39**, 17446–17457.

124 X. Song, D. Tian, Y. Qiu, X. Sun, B. Jiang, C. Zhao, Y. Zhang, L. Fan and N. Zhang, *Adv. Funct. Mater.*, 2022, **32**, 2109413.

125 A. Bhargav, C. H. Chang, Y. Fu and A. Manthiram, *ACS Appl. Mater. Interfaces*, 2019, **11**, 6136–6142.

126 L. Chen, G. Cao, Y. Li, G. Zu, R. Duan, Y. Bai, K. Xue, Y. Fu, Y. Xu, J. Wang and X. Li, *Nano-Micro Lett.*, 2024, **16**, 1–33.

127 H. Gamo, K. Hikima and A. Matsuda, *ACS Omega*, 2023, **8**, 45557–45565.

128 M. U. M. Patel, I. Arčon, G. Aquilanti, L. Stievano, G. Mali and R. Dominko, *ChemPhysChem*, 2014, **15**, 894–904.

129 M. Abe, F. Kaneko, N. Ishiguro, T. Kubo, F. Chujo, Y. Tamenori, H. Kishimoto and Y. Takahashi, *J. Phys. Chem. C*, 2022, **126**, 14047–14057.

130 R. Li, D. Rao, J. Zhou, G. Wu, G. Wang, Z. Zhu, X. Han, R. Sun, H. Li, C. Wang, W. Yan, X. Zheng, P. Cui, Y. Wu, G. Wang and X. Hong, *Nat. Commun.*, 2021, **12**, 1–8.

131 Q. Guo, K. C. Lau and R. Pandey, *Mater. Adv.*, 2021, **2**, 6403–6410.

132 U. Zubair, K. Jori, J. E. Thomas, J. Amici, C. Francia and S. Bodoardo, *J. Power Sources*, 2023, **580**, 233457.

133 G. Ai, Q. Hu, L. Zhang, K. Dai, J. Wang, Z. Xu, Y. Huang, B. Zhang, D. Li, T. Zhang, G. Liu and W. Mao, *ACS Appl. Mater. Interfaces*, 2019, **11**, 33987–33999.

134 L. Shi, S. M. Bak, Z. Shadike, C. Wang, C. Niu, P. Northrup, H. Lee, A. Y. Baranovskiy, C. S. Anderson, J. Qin, S. Feng, X. Ren, D. Liu, X. Q. Yang, F. Gao, D. Lu, J. Xiao and J. Liu, *Energy Environ. Sci.*, 2020, **13**, 3620–3632.

135 X. Yu, H. Pan, Y. Zhou, P. Northrup, J. Xiao, S. Bak, M. Liu, K.-W. Nam, D. Qu, J. Liu, T. Wu, X.-Q. Yang, X. Yu, Y. Zhou, P. Northrup, S. Bak, M. Liu, X.-Q. Yang, H. Pan, J. Xiao, J. Liu, W. K. Nam, D. Qu and T. Wu, *Adv. Energy Mater.*, 2015, **5**, 1500072.

136 F. Luna-Lama, A. Caballero and J. Morales, *Sustainable Energy Fuels*, 2022, **6**, 1568–1586.

137 L. Shi, S. M. Bak, Z. Shadike, C. Wang, C. Niu, P. Northrup, H. Lee, A. Y. Baranovskiy, C. S. Anderson, J. Qin, S. Feng, X. Ren, D. Liu, X. Q. Yang, F. Gao, D. Lu, J. Xiao and J. Liu, *Energy Environ. Sci.*, 2020, **13**, 3620–3632.

138 M. Li, W. Liu, D. Luo, Z. Chen, K. Amine and J. Lu, *ACS Energy Lett.*, 2022, **7**, 577–582.

139 C. Li, Y. Li, Y. Fan, F. Wang, T. Lei, W. Chen, A. Hu, L. Xue, J. Huang, C. Wu, C. Yang, Y. Hu and Y. Yan, *Small*, 2022, **18**, 2106657.

140 X. Guo, J. Zhang, L. Yuan, B. Xi, F. Gao, X. Zheng, R. Pan, L. Guo, X. An, T. Fan and S. Xiong, *Adv. Energy Mater.*, 2023, **13**, 2204376.

141 V. K. Tomer, R. Malik, J. Tjong and M. Sain, *Coord. Chem. Rev.*, 2023, **481**, 215055.

142 A. J. Cowan and L. J. Hardwick, *Annu. Rev. Anal. Chem.*, 2019, **12**, 323–346, DOI: **10.1146/annurev-anchem-061318-115303**.

143 J. Lim, K. K. Lee, C. Liang, K. H. Park, M. Kim, K. Kwak and M. Cho, *J. Phys. Chem. B*, 2019, **123**, 6651–6663.

144 M. Weiling, F. Pfeiffer, M. Baghernejad, M. Weiling, F. Pfeiffer and M. Baghernejad, *Adv. Energy Mater.*, 2022, **12**, 2202504.

145 S. Nowak and M. Winter, *J. Anal. At. Spectrom.*, 2017, **32**, 1833–1847.

146 L. Meyer, N. Saqib and J. Porter, *J. Electrochem. Soc.*, 2021, **168**, 090561.

147 M. A. Weret, C. F. J. Kuo, W. N. Su, T. S. Zeleke, C. J. Huang, N. A. Sahalie, T. A. Zegeye, Z. T. Wondimkun, F. W. Fenta, B. A. Jote, M. C. Tsai and B. J. Hwang, *J. Power Sources*, 2022, **541**, 231693.

148 L. Xue, Y. Li, A. Hu, M. Zhou, W. Chen, T. Lei, Y. Yan, J. Huang, C. Yang, X. Wang, Y. Hu and J. Xiong, *Small Struct.*, 2022, **3**, 2100170.

149 R. Zhang, Y. Wu, Z. Chen, Y. Wang, J. Zhu and X. Zhuang, *J. Mater. Chem. A*, 2023, **11**, 19195–19209.

150 X. Q. Cheng, H. J. Li, Z. X. Zhao, Y. Z. Wang and X. M. Wang, *New Carbon Mater.*, 2021, **36**, 93–105.

151 É. A. Santos, R. C. Fernandes, R. Vicentini, J. P. Aguiar, L. M. Da Silva and H. Zanin, *J. Energy Storage*, 2023, **71**, 108203.

152 Z. Pan, D. J. L. Brett, G. He, I. P. Parkin, Z. Pan, G. He, I. P. Parkin and D. J. L. Brett, *Adv. Energy Mater.*, 2022, **12**, 2103483.

153 L. Zhang, T. Qian, X. Zhu, Z. Hu, M. Wang, L. Zhang, T. Jiang, J. H. Tian and C. Yan, *Chem. Soc. Rev.*, 2019, **48**, 5432–5453.

154 J. H. Tian, T. Jiang, M. Wang, Z. Hu, X. Zhu, L. Zhang, T. Qian and C. Yan, *Small Methods*, 2020, **4**, 1900467.

155 C. Dillard, S. H. Chung, A. Singh, A. Manthiram and V. Kalra, *Mater. Today Energy*, 2018, **9**, 336–344.

156 H. Du, S. Li, H. Qu, B. Lu, X. Wang, J. Chai, H. Zhang, J. Ma, Z. Zhang and G. Cui, *J. Membr. Sci.*, 2018, **550**, 399–406.

157 J. Liu, J. Wang, L. Zhu, X. Chen, Q. Ma, L. Wang, X. Wang and W. Yan, *Chem. Eng. J.*, 2021, **411**, 128540.

158 Z. Liang, J. Shen, X. Xu, F. Li, J. Liu, B. Yuan, Y. Yu and M. Zhu, *Adv. Mater.*, 2022, **34**, 2200102.

159 H. Li, C. Chen, Y. Yan, T. Yan, C. Cheng, D. Sun and L. Zhang, *Adv. Mater.*, 2021, **33**, 2105067.

160 S. A. Bonke, T. Risse, A. Schnegg and A. Brückner, *Nat. Rev. Methods Primers*, 2021, **1**, 1–20.

161 L. Galazzo and E. Bordignon, *Prog. Nucl. Magn. Reson. Spectrosc.*, 2023, **134–135**, 1–19.

162 T. Insinna, E. N. Bassey, K. Märker, A. Collauto, A. L. Barra and C. P. Grey, *Chem. Mater.*, 2023, **35**, 5497–5511.

163 Z. Ye, Y. Jiang, L. Li, F. Wu and R. Chen, *Adv. Mater.*, 2022, **34**, 2109552.

164 Y. Zhou, M. Su, X. Yu, Y. Zhang, J. G. Wang, X. Ren, R. Cao, W. Xu, D. R. Baer, Y. Du, O. Borodin, Y. Wang, X. L. Wang, K. Xu, Z. Xu, C. Wang and Z. Zhu, *Nat. Nanotechnol.*, 2020, **15**, 224–230.

165 L. Cressa, Y. Sun, D. Andersen, M. Gerard, O. De Castro, D. Kopljar, M. Nojabaee, K. A. Friedrich, G. Schmitz, T. Wirtz and S. Eswara, *Anal. Chem.*, 2023, **95**, 9932–9939.

166 K. Schaepe, H. Jungnickel, T. Heinrich, J. Tentschert, A. Luch and W. E. S. Unger, *Characterization of Nanoparticles: Measurement Processes for Nanoparticles*, 2020, pp. 481–509.

167 H. Mei, T. S. Laws, T. Terlier, R. Verduzco and G. E. Stein, *J. Polym. Sci.*, 2022, **60**, 1174–1198.

168 K. Bagheri, M. Deschamps and E. Salager, *Curr. Opin. Colloid Interface Sci.*, 2023, **64**, 101675.

169 X. Liu, Z. Liang, Y. Xiang, M. Lin, Q. Li, Z. Liu, G. Zhong, R. Fu and Y. Yang, *Adv. Mater.*, 2021, **33**, 2005878.

170 N. Leifer, D. Aurbach and S. G. Greenbaum, *Prog. Nucl. Magn. Reson. Spectrosc.*, 2024, **142–143**, 1–54.

171 J. B. Fritzke, S. Dey, C. A. O'Keefe and C. P. Grey, *ECS Meeting Abstracts*, 2023, MA2023-02, 2692.

172 S. Duhan and V. K. Tomer, in *Advanced Sensor and Detection Materials*, ed. A. Tiwari and M. M. Demir, John Wiley and Sons Ltd, 2014, pp. 149–192.

173 V. K. Tomer, S. Duhan, P. V. Adhyapak and I. S. Mulla, *J. Am. Ceram. Soc.*, 2015, **98**, 741–747.

174 V. K. Tomer and S. Duhan, *Appl. Phys. Lett.*, 2015, **106**, 063105.

175 R. Malik, V. K. Tomer, M. Sain and Z. Chen, *Renewable Sustainable Energy Rev.*, 2023, **181**, 113348.

176 B. Liu and V. S. Thoi, *Chem. Commun.*, 2022, **58**, 4005–4015.

177 R. Yan, B. Mishra, M. Traxler, J. Roeser, N. Chaoui, B. Kumbhakar, J. Schmidt, S. Li, A. Thomas and P. Pachfule, *Angew. Chem., Int. Ed.*, 2023, **62**, e202302276.

178 X. Li, K. Zhang, Z. Li, Y. Yan, Y. Yuan, L. Ma, K. Xie and K. Ping Loh, *Angew. Chem., Int. Ed.*, 2023, **62**, e202217869.

179 A. Shafique, V. S. Rangasamy, A. Vanhulsel, M. Safari, M. K. Van Bael, A. Hardy and S. Sallard, *Electrochim. Acta*, 2020, **360**, 136993.

180 D. Hou, F. Bai, P. Dong, J. Chen, Y. Zhang, F. Meng, Z. Zhang, C. Zhang, Y. Zhang and J. Hu, *J. Power Sources*, 2023, **584**, 233599.

181 M. G. Bason, T. Coussens, M. Withers, C. Abel, G. Kendall and P. Krüger, *J. Power Sources*, 2022, **533**, 231312.

182 D. Atkins, E. Ayerbe, A. Benayad, F. G. Capone, E. Capria, I. E. Castelli, I. Cekic-Laskovic, R. Ciria, L. Dudy, K. Edström, M. R. Johnson, H. Li, J. M. G. Lastra, M. L. De Souza, V. Meunier, M. Morcrette, H. Reichert, P. Simon, J. P. Rueff, J. Sottmann, W. Wenzel and A. Grimaud, *Adv. Energy Mater.*, 2022, **12**, 2102687.

183 Z. Huang, Y. Zhou, Z. Deng, K. Huang, M. Xu, Y. Shen and Y. Huang, *ACS Appl. Mater. Interfaces*, 2023, **15**, 8217–8223.

184 Z. Deng, Z. Huang, Y. Shen, Y. Huang, H. Ding, A. Luscombe, M. Johnson, J. E. Harlow, R. Gauthier and J. R. Dahn, *Joule*, 2020, **4**, 2017–2029.

185 A. Niemöller, P. Jakes, R. A. Eichel and J. Granwehr, *Sci. Rep.*, 2018, **8**, 1–7.

186 H. Zhou, A. S. Alujjage, M. Terese, C. Fear, T. Joshi, V. R. Rikka, J. A. Jeevarajan and P. P. Mukherjee, *Appl. Energy*, 2025, **377**, 124465.

187 T. Bond, R. Gauthier, S. Gasilov and J. R. Dahn, *J. Electrochem. Soc.*, 2022, **169**, 080531.

188 Y. J. Xu, B. Wang, Y. Wan, Y. Sun, W. L. Wang, K. Sun, L. J. Yang, H. Hu and M. B. Wu, *New Carbon Mater.*, 2023, **38**, 678–693.

189 Y. S. Duh, Y. Sun, X. Lin, J. Zheng, M. Wang, Y. Wang, X. Lin, X. Jiang, Z. Zheng, S. Zheng and G. Yu, *J. Energy Storage*, 2021, **41**, 102888.

190 G. Xu, L. Huang, C. Lu, X. Zhou and G. Cui, *Energy Storage Mater.*, 2020, **31**, 72–86.

191 Y. S. Duh, X. Liu, X. Jiang, C. S. Kao, L. Gong and R. Shi, *J. Energy Storage*, 2020, **30**, 101422.

192 D. Ouyang, M. Chen, J. Weng, K. Wang, J. Wang and Z. Wang, *J. Energy Chem.*, 2023, **81**, 543–573.

193 L. Huang, T. Lu, G. Xu, X. Zhang, Z. Jiang, Z. Zhang, Y. Wang, P. Han, G. Cui and L. Chen, *Joule*, 2022, **6**, 906–922.

194 L. Vásárhelyi, Z. Kónya, A. Kukovecz and R. Vajtai, *Mater. Today Adv.*, 2020, **8**, 100084.

195 Z. Yan, L. Wang, H. Zhang and X. He, *Adv. Energy Mater.*, 2024, **14**, 2303206.

196 X. Wan, X. Xu, F. Li, X. Song, C. Peng and J. Liu, *Small Struct.*, 2024, **5**, 2300196.

197 J. Le Houx and D. Kramer, *Energy Rep.*, 2021, **7**, 9–14.

198 H. Li and W. Wang, *Curr. Opin. Electrochem.*, 2023, **41**, 101376.

199 J. H. Um, S. J. Kim, J. H. Hyun, M. Kim, S. H. Lee and S. H. Yu, *Acc. Chem. Res.*, 2023, **56**, 440–451.

200 J. H. Tian, T. Jiang, T. Wang, Z. Hu, X. Zhu, L. Zhang, T. Qian and C. Yan, *Small Methods*, 2020, **4**, 1900467.

201 D. Cao, Y. Zhang, T. Ji and H. Zhu, *MRS Bull.*, 2023, **48**, 1257–1268.

202 H. Wang, D. Ning, L. Wang, H. Li, Q. Li, M. Ge, J. Zou, S. Chen, H. Shao, Y. Lai, Y. Zhang, G. Xing, W. K. Pang and Y. Tang, *Small*, 2022, **18**, 2107491.

203 S. Zhou, K. Liu, Y. Ying, L. Chen, G. Meng, Q. Zheng, S. G. Sun and H. G. Liao, *Curr. Opin. Electrochem.*, 2023, **41**, 101374.

204 D. Yang, Y. X. A. Ng, K. Zhang, Q. Chang, J. Chen, T. Liang, S. Cheng, Y. Sun, W. Shen, E. H. Ang, H. Xiang and X. Song, *ACS Appl. Mater. Interfaces*, 2023, **15**, 20583–20602.

205 H. Li and W. Wang, *Curr. Opin. Electrochem.*, 2023, **41**, 101376.

206 R. Zhang, Y. Wu, Z. Chen, Y. Wang, J. Zhu and X. Zhuang, *J. Mater. Chem. A*, 2023, **11**, 19195–19209.

207 L. Xue, Y. Li, A. Hu, M. Zhou, W. Chen, T. Lei, Y. Yan, J. Huang, C. Yang, X. Wang, Y. Hu and J. Xiong, *Small Struct.*, 2022, **3**, 2100170.

208 L. Xue, Y. Li, A. Hu, M. Zhou, W. Chen, T. Lei, Y. Yan, J. Huang, C. Yang, X. Wang, Y. Hu and J. Xiong, *Small Struct.*, 2022, **3**, 2100170.

209 K. Bagheri, M. Deschamps and E. Salager, *Curr. Opin. Colloid Interface Sci.*, 2023, **64**, 101675.

210 A. P. Black, A. Sorrentino, F. Fauth, I. Yousef, L. Simonelli, C. Frontera, A. Ponrouch, D. Tonti and M. R. Palacín, *Chem. Sci.*, 2023, **14**, 1641–1665.

211 M. Pin, J. Choi, J. H. Chang, A. S. Schenk, J. Han, S. Wacławek, Y. Kim and J. Y. Cheong, *Energy Storage Mater.*, 2024, **73**, 103798.

212 K. Wang, D. Luo, Q. Ma, X. Lai, L. He and Z. Chen, *Energy Technol.*, 2024, **12**, 2400199.

213 M. M. Amaral, C. G. Real, V. Y. Yukuhiro, G. Doubek, P. S. Fernandez, G. Singh and H. Zanin, *J. Energy Chem.*, 2023, **81**, 472–491.

214 Y. S. Byeon, W. Lee, S. Park, D. Kim, J. Jung, M. S. Park and W. S. Yoon, *Small Sci.*, 2024, 2400165.

215 É. A. Santos, M. M. Amaral, B. S. Damasceno, L. M. Da Silva, H. G. Zanin, J. N. Weker and C. B. Rodella, *Nano Energy*, 2024, **130**, 110098.

216 M. A. Bañares and M. Daturi, *Catal. Today*, 2023, **423**, 114255.

217 F. Strauss, D. Kitsche, Y. Ma, J. H. Teo, D. Goonetilleke, J. Janek, M. Bianchini and T. Brezesinski, *Adv. Energy Sustainability Res.*, 2021, **2**, 2100004.

218 J. H. Um and S. H. Yu, *Adv. Energy Mater.*, 2021, **11**, 2003004.

219 T. Zheng, M. Muneeswara, H. Bao, J. Huang, L. Zhang, D. S. Hall, S. T. Boles and W. Jin, *ChemElectroChem*, 2024, **11**, e202400065.